

# **Stony Brook University**



OFFICIAL COPY

**The official electronic file of this thesis or dissertation is maintained by the University Libraries on behalf of The Graduate School at Stony Brook University.**

**© All Rights Reserved by Author.**

**Evolution of the One-Quadrupole  
Phonon Mixed-Symmetry State in the  
 $A = 140$  Mass Region**

A Dissertation Presented

by

**Tan Ahn**

to

The Graduate School

in Partial Fulfillment of the Requirements

for the Degree of

**Doctor of Philosophy**

in

**Physics**

Stony Brook University

May 2008

**Stony Brook University**

The Graduate School

**Tan Ahn**

We, the dissertation committee for the above candidate for the Doctor of Philosophy degree, hereby recommend acceptance of this dissertation.

Gene Sprouse – Dissertation Advisor  
Distinguished Professor, Department of Physics and Astronomy

Thomas Kuo – Chairperson of Defense  
Professor, Department of Physics and Astronomy

Harald Metcalf  
Professor, Department of Physics and Astronomy

Norbert Pietralla  
Professor, Institut für Kernphysik  
Technische Universität Darmstadt

Jiangyong Jia  
Assistant Professor, Department of Chemistry  
Stony Brook University

This dissertation is accepted by the Graduate School.

Lawrence Martin  
Dean of the Graduate School

Abstract of the Dissertation

**Evolution of the One-Quadrupole Phonon  
Mixed-Symmetry State in the  $A = 140$  Mass  
Region**

by

**Tan Ahn**

**Doctor of Philosophy**

in

**Physics**

Stony Brook University

2008

Collective excitations are a common phenomena in atomic nuclei. These excitations arise from the coherent movement of many particles in the nucleus. A special class of collective excitations, called mixed-symmetry states, which are defined in the Interacting Boson Model-2, have been found in atomic nuclei and are interpreted geometrically as an out of phase motion of protons and neutrons. Together with collective excitations in which the protons and neutrons move in phase, these states can be used as building blocks for a general description of collective phenomena in nuclei. Mixed-symmetry states are also sensitive to the strength of the residual proton-neutron quadrupole interaction in the valence shell and thus their properties are important in constraining the strength of this interaction. A number of one-quadrupole phonon mixed-symmetry ( $2_{1,ms}^+$ ) states have been found in vibrational nuclei in the  $A = 140$  mass region. To better understand the evolution of mixed-symmetry states in this mass region, experiments were

done to identify the  $2_{1,\text{ms}}^+$  state in the nuclides  $^{134}\text{Xe}$  and  $^{136}\text{Ce}$  using the technique of Coulomb excitation in inverse kinematics. Together with standard techniques in gamma-ray spectroscopy, absolute electromagnetic transition strengths were measured and the  $2_{1,\text{ms}}^+$  states in these nuclides were identified. The evolution of the energy of the  $2_{1,\text{ms}}^+$  state in the  $N = 80$  isotones shows an increase in the proton-neutron interaction in the valence shell. The energy of these states were fitted by performing an Interacting Boson Model-2 calculation, which shows that the evolution in energy can be modelled with an appropriate set of terms in the IBM-2 Hamiltonian. The  $2_{1,\text{ms}}^+$  states in the  $N = 78$  isotones show a similar behavior to the corresponding states in the  $N = 80$  isotones and show that the mixed-symmetry states are sensitive to the residual proton-neutron interaction in this mass region.

To my loving parents, Sarah and Young

# Contents

<b>List of Figures</b>	<b>viii</b>
<b>List of Tables</b>	<b>xi</b>
<b>Acknowledgements</b>	<b>xii</b>
<b>1 Introduction</b>	<b>1</b>
1.1 Brief History of Nuclear Physics . . . . .	1
1.2 Scientific Motivation . . . . .	3
<b>2 The Interacting Boson Model and Mixed-Symmetry States</b>	<b>6</b>
2.1 Interacting Boson Model-1 . . . . .	6
2.1.1 Boson Creation and Annihilation Operators . . . . .	6
2.1.2 Operators and Basis States . . . . .	8
2.2 Interacting Boson Model-2 . . . . .	11
2.2.1 Full and Mixed Proton Neutron Symmetry . . . . .	14
2.2.2 Signature of Mixed-Symmetry States . . . . .	18
<b>3 Coulomb Excitation</b>	<b>21</b>
3.1 Semi-Classical Theory . . . . .	22
3.1.1 Coulomb Excitation Cross Sections . . . . .	25
3.1.2 Angular Distribution of $\gamma$ rays . . . . .	28
<b>4 Experiment and Data Analysis</b>	<b>31</b>
4.1 Experiment . . . . .	31
4.2 Data Analysis . . . . .	37
4.2.1 Efficiency Calibration . . . . .	37
4.2.2 Doppler Correction . . . . .	38
4.2.3 Room Background Subtraction . . . . .	42
4.2.4 Measuring Angular Distributions of $\gamma$ Rays . . . . .	44

4.2.5	Transition Matrix Elements from Coulomb Excitation Cross Sections . . . . .	51
4.2.6	Coincidence Analysis . . . . .	55
<b>5</b>	<b>Evolution of Mixed-Symmetry States</b>	<b>61</b>
5.1	$N = 80$ Isotones . . . . .	61
5.1.1	Identification of the $2_{1,ms}^+$ State in $^{134}\text{Xe}$ . . . . .	61
5.1.2	Phenomenological fit . . . . .	61
5.1.3	IBM-2 Calculation . . . . .	64
5.1.4	Evolution of Transition Strengths . . . . .	66
5.2	$N = 78$ Isotones . . . . .	67
5.2.1	Identification of the $2_{1,ms}^+$ State in $^{136}\text{Ce}$ . . . . .	67
5.2.2	Evolution of the $2_{1,ms}^+$ State . . . . .	67
<b>6</b>	<b>Summary</b>	<b>69</b>
6.1	Outlook . . . . .	69
	<b>Bibliography</b>	<b>72</b>
<b>A</b>	<b>Multipole Operators and Mixing Ratios</b>	<b>76</b>
A.1	Gamma Emission . . . . .	76
A.2	Multipole Mixing Ratios . . . . .	78



# List of Figures

1.1	Nuclides in the $A = 140$ mass region are shown. The green boxes indicate nuclides where mixed-symmetry states have been identified. The pink boxes indicate the nuclides studied in this present work. The magenta box indicates the nuclide where a mixed-symmetry state has been tentatively identified. The $Z = 50$ and $N = 82$ shell closures are indicated by lines. . . .	5
2.1	Example of IBM-2 states in $u(5)$ limit. Building blocks of collective excitations. . . . .	17
2.2	Geometric interpretation of mixed-symmetry states are shown. The figure represents a snapshot of the nucleus in time where the red indicates the proton fluid and the blue represents the neutron fluid. Part (a) represents the out of phase vibration for spherical nuclei and (b) represents the vibration of protons and neutrons with respect to each other for prolate or oblate deformed nuclei. . . . .	18
2.3	Figure showing the signature $M1$ decays of mixed-symmetry states. . . . .	20
3.1	The scattering of the projectile off the target is shown. Classically for elastic scattering, the path of the projectile is a hyperbola where $\theta$ is the scattering angle and $b$ is the impact parameter.	22
3.2	A plot showing the relation between the angles of the scattered projectile and target in the center of mass and lab frames. . .	27
3.3	The reference frame for $(i) = (0)$ is shown. The $Z$ axis bisects the asymptotes of the hyperbolic path of the projectile as shown. The $Y$ and $Z$ axes define the plane that contains the path of the projectile. . . . .	29
3.4	The reference frame for $(i) = (3)$ is shown. The $Z$ axis is parallel to the initial direction of the projectile and the $X$ and $Z$ axes define the plane of the projectile's path. . . . .	30

4.1	The a drawing of the Gammasphere array is shown. It consists of 110 HPGe detectors arranged spherically. The faces of the detectors form a 122-element polyhedron consisting of 110 hexagons and 12 pentagons. (Figure from Ref. [50]) . . . . .	32
4.2	A schematic diagram of Gammasphere HPGe detectors. It consists of a HPGe crystal, BGO anti-Compton elements, photomultipliers for the BGO elements, Hevimet collimators, detector electronics, and a liquid nitrogen dewar, which stores liquid nitrogen for cooling the HPGe crystal. (Figure from Ref. [50]) . . . . .	33
4.3	Two energy spectra are shown for data obtained from a $^{60}\text{Co}$ source with and without Compton supression. (Figure from Ref. [50]) . . . . .	34
4.4	An energy spectrum for $^{134}\text{Xe}$ for the sum of all Gammasphere detectors. . . . .	35
4.5	An energy spectrum for $^{136}\text{Ce}$ for the sum of all Gammasphere detectors. . . . .	36
4.6	Level scheme for the observed transitions and corresponding levels in $^{134}\text{Xe}$ . . . . .	37
4.7	Level scheme for the observed transitions and corresponding levels in $^{136}\text{Ce}$ . . . . .	38
4.8	The measured relative efficiency and the fitted efficiency curve for the set of Gammasphere detectors at $90^\circ$ . . . . .	39
4.9	Shown is the segmentation of the outer electrode of segmented Gammasphere detectors. A $\gamma$ ray hitting different parts of the detector will have different Doppler shifts. (Figure from Ref. [50]) . . . . .	41
4.10	Spectrum of peaks from one of the Gammasphere detectors separated into left hit, center hit, and right hit is plotted in red, green, and blue, respectively. . . . .	41
4.11	Part of the time-energy matrix is shown. The peaks corresponding to room background and Coulomb excitation can be seen. . . . .	43
4.12	Illustration of time spectrum and the beam and background gates set on it. . . . .	44
4.13	A parts of a Doppler-uncorrected energy spectrum are shown with and without subtraction using time gates. Part (a) shows the 1461-keV peak from the decay of naturally occurring $^{40}\text{K}$ . Part (b) shows it subtracted. Part (c) shows two background lines, one of which is the peak coming from the decay of Th. Part (d) shows the Th line subtracted while the other remains. . . . .	45
4.14	The decay of a $2^+$ excited state. . . . .	47

4.15	The measured and fitted angular distribution function $W(\theta)$ for the 1614-keV transition in $^{134}\text{Xe}$ . . . . .	48
4.16	The relative population of $M$ states of $2^+$ states of $^{134}\text{Xe}$ is shown.	50
4.17	The measured and fitted angular distribution function $W(\theta)$ for the 767-keV transition in $^{134}\text{Xe}$ . . . . .	50
4.18	A $2^+$ state decaying to the $2_1^+$ state and $0_1^+$ ground state. The matrix elements for the transitions, the quadrupole moments of the states $Q_0$ are input parameters of the program. The branching ratio and multipole mixing ratio $\delta$ put constraints on the value of the matrix elements. . . . .	52
4.19	The measured transition strengths in $^{134}\text{Xe}$ . The values plotted for the transitions from the $2_3^+$ and $2_4^+$ states are the transition strengths that correspond to the smaller of two possible $\delta$ values.	55
4.20	The measured transition strengths in $^{136}\text{Ce}$ . . . . .	58
4.21	A two-dimensional view of the symmetric $E_\gamma$ - $E_\gamma$ matrix of $^{134}\text{Xe}$ .	59
4.22	A gate on the 921-keV transition in $^{134}\text{Xe}$ . . . . .	60
5.1	A phenomenological fit for the energy of the $2_{1,\text{ms}}^+$ state in the $N = 80$ isotones . . . . .	62
5.2	Shown are the energies of $2^+$ states in the $N = 80$ isotones along with the calculated energy levels using the IBM-2 program NPBOS. . . . .	65
5.3	The $M1$ transition strengths are shown for the $2^+ \rightarrow 2_1^+$ transition in the $N = 80$ isotones. . . . .	66
5.4	The $2_1^+$ states and $2_{1,\text{ms}}^+$ states of the $N = 78$ isotones. . . . .	67
5.5	The $M1$ transition strengths for the $2^+ \rightarrow 2_1^+$ transition in the $N = 78$ isotones. . . . .	68
6.1	The isotopes $^{130}\text{Te}$ and $^{132}\text{Te}$ would extend the known data on mixed-symmetry states in the $A = 140$ mass region. . . . .	71

# List of Tables

4.1	Table of $\rho_n$ coefficients for $2^+$ states in $^{134}\text{Xe}$ . The values marked with an * were calculated from first-order perturbation theory for a beam energy of 435 MeV. . . . .	49
4.2	A compilation of the measured quantities in $^{134}\text{Xe}$ . . . . .	56
4.3	A compilation of the measured quantities in $^{136}\text{Ce}$ . . . . .	57

# Acknowledgements

I would like to gratefully acknowledge and thank Norbert Pietralla for all his guidance and support in my studies and for allowing me the opportunity to continue with my dissertation research in Germany. I am grateful for all the support he has given me in my various academic endeavors during the past 4 years.

I especially would like to thank Gene Sprouse without whom I can safely say I would not have been able to continue and pursue research in physics. He has been instrumental in so many ways in allowing me to continue my studies at Stony Brook for which I am very grateful.

I would like to gratefully acknowledge the late Dave Fossan and Kris Starosta who have given me the opportunity to work in nuclear structure physics, guided me in the early years, and have shown me great support in continuing my studies.

I thank former members of the Stony Brook nuclear structure group Takeshi Koike and Georgi Rainovski for all their guidance and help in research.

There are many from the faculty at Stony Brook that have helped me in numerous ways, whether it was through advising as an undergraduate/graduate director, supporting me through a letter of recommendation, or giving informal advice, etc., for which I would like to thank Tom Kuo, Harald Metcalf, Lázlo Mihaly, Gerry Brown, Emilio Mendez, John Hobbs, Paul Grannis, Ismael Zahed, Peter Kahn, Peter Stephens, and Philip Allen.

I would also like to acknowledge and thank Laurent Coquard, who has calculated the tentative  $M1$  strengths in  $^{132}\text{Xe}$  and has also run the GOSIA calculations for  $^{134}\text{Xe}$  and  $^{136}\text{Ce}$ .

Finally, I would like to thank Mike Riley, the author of Ref. [50], for permission to reproduce the figures found in Figs. 4.1, 4.2, 4.3, and 4.10.

# Chapter 1

## Introduction

### 1.1 Brief History of Nuclear Physics

Nuclear physics has been an active field of research since the discovery of the nucleus. Ernest Rutherford found that most of all matter was concentrated in a very small core at the center of the atom in 1911 [1]. Perhaps the next great milestone was the discovery of the neutron by the associate and doctoral student of Rutherford, James Chadwick in 1932 [2]. It is noteworthy that by this time special relativity, quantum mechanics, and the relativistic formulation of quantum mechanics were already developed. The existence of the positron was postulated by P. A. M. Dirac in his relativistic formulation of quantum mechanics in 1928 [3, 4] and it was subsequently discovered in 1932 by Carl Anderson [5], the same year the neutron was discovered. I would thus list the finding of the neutron as a relatively modern discovery. The proton and neutron have since been used as the fundamental building blocks in describing the nature of the atomic nucleus to this day.

A number of models have been developed to describe the large array of phenomena and properties displayed by atomic nuclei. The liquid drop model, first proposed by George Gamow in 1928 [6], viewed the nucleus as drop of liquid whose constituent particles were held together by surface tension. This model was able to describe some bulk properties of nuclei. Using the ideas of the liquid drop model, von Weizsäcker developed a semi-empirical mass formula [7] to predict nuclear masses. A large breakthrough in nuclear theory came in 1949 when Maria Goeppert-Mayer [8] and independently J. Jensen, O. Haxel, and H. Suess [9] were able to explain the magic numbers in nuclei, where nuclei would exhibit an increased stability, by including a spin-orbit interaction term in a Hamiltonian that considered all nucleons to be orbiting essentially freely in an average field created by all the other nucleons. The magic numbers

correspond to closed shells in nuclei analogous to the filling of electron shells in atoms. Excited states were found that correspond to the excitation of a nucleon into an orbit of a higher lying shell as predicted by the model. The shell model, as this model is called, has been one of the most fundamental ways to describe atomic nuclei. It has since been used extensively in the analysis of experimental data.

Apart from the single-particle excitations found in nuclei, another type of excitation, collective excitation, was soon explained. In 1950, Rainwater observed that spherical nuclei could easily be deformed [10]. This led the way in the 1950's for more ground breaking work done by Aage Bohr and Ben Mottelsohn [11, 12] and also H. L. Hill and J. A. Wheeler [13] when they presented models for collective motion in nuclei. These models used shapes to parameterize the nucleus and used their dynamics to derive the collective phenomena that was observed. Since the discoveries of single-particle and collective motion, these have been the two ways in which excitations in nuclei have been classified. The interplay between single-particle and collective degrees of freedom has long been and continues to be an active field of study. One example is perhaps a variation of the shell model, which was proposed by S. G. Nilsson in 1955 [14] where he considered the average potential of the shell model to be deformed. This led to the idea of changing shell structure with deformation.

In 1975, the Interacting Boson Model, the model that was used in this present work, was proposed by F. Iachello and A. Arima [15] where interacting bosons are used to describe collective excitations in nuclei. From the symmetry properties of the model's boson operators, three types of idealized nuclei were found whose properties can be calculated analytically. These three limits of nuclei can be used as benchmarks with which to classify different nuclei. It was found that different regions of the nuclear chart exhibit properties that are similar to one of these idealized limits.

The above account of nuclear physics is very brief and highlights only a few of the main accomplishments in nuclear physics in the twentieth century. Although brief, it can be seen that there is not one single comprehensive theory in nuclear physics, but several models tailored to describe specific phenomena. A quote taken from the book of Eisenbud and Wigner [16] published in 1958 describes the state of nuclear theory in the following way,

It is easy to appreciate the reasons for the present formlessness of nuclear theory. Internucleon forces are not yet completely known and it is clear that they have a complex character. Even the consequences of a simple interaction are difficult to obtain for a system containing a large but finite number of particles. A good

deal of effort has been expended, therefore, in the search for simple models in terms of which the broad regularities satisfied by nuclei could be understood. This search has led to a number of interesting but only partially successful models; these have proved very fruitful for the stimulation of experimental research, and for the development of further ideas on nuclear structure. One can hope that future investigations will clarify the limitations of these models and provide an understanding of the validity of different models for different groups of phenomena.

Although written in 1958, the ideas set forth in this quote still serve as an apt description of present day research in nuclear physics. It is with the ideas of better understanding the “broad regularities satisfied by nuclei” and “understanding the validity of different models for different groups of phenomena” the topic of this present work is introduced. One of the broad regularities in nuclei that will be investigated is the existence of a certain class of collective excitations called mixed-symmetry states defined within the Interacting Boson Model. The data obtained from the experimental investigations of these states will help elucidate the extent of the validity of the Interacting Boson Model.

## 1.2 Scientific Motivation

A certain class of collective states arise in the proton-neutron version of the Interacting Boson Model called mixed-symmetry states [17], which can be thought of as states in which the protons and neutrons oscillate out of phase with respect to one another. This mode of excitation should be sensitive to the proton-neutron interaction in the valence shell because of its isovector character. Seeing how these states evolve as a function of proton and neutron number can give insight into the strength of the proton-neutron interaction for a given mass region.

The proton-neutron interaction in the valence shell of nuclei has been attributed as being responsible for the formation of collectivity in nuclei [18, 19]. There have been fits made for the strength of this interaction using phenomenological models for a number of nuclei, especially in the  $A = 140$  mass region [20, 21], but data are still sparse.

The first experimentally observed mixed-symmetry state was in  $^{156}\text{Gd}$  by Bohle et al. [22] using the method of electron scattering to measure  $M1$  transition strengths. These were  $1^+$  states in deformed nuclei and came to be known as the scissors mode as the geometrical interpretation was a vibration of the protons and neutrons that resembles the opening and closing of a pair



of scissors. Reviews on the study of the scissors mode can be found in Refs. [23, 24]. The first experimentally proposed mixed-symmetry state in a vibrational nucleus was by Hamilton in 1984 [25] based on a measurement of multipole mixing ratios. Since then mixed-symmetry states have been found in several regions of the nuclear chart, notably in the  $A = 90$  and  $A = 140$  mass regions. A comprehensive review of presently known mixed-symmetry states in vibrational nuclei identified by the measurement of absolute transition strengths is given in Ref. [26].

### **Vibrational Mixed-Symmetry States in the $A = 140$ Mass Region**

Though many mixed-symmetry states have been identified in the past two decades, data on mixed symmetry states is still scarce due to the difficulty in measuring absolute transition strengths for the decay of short-lived nuclear states. A number of one-phonon  $2^+$  mixed-symmetry states have been found in the  $A = 140$  mass region [25, 27–33]. This present work focuses on extending the data on mixed-symmetry states in this mass region by identifying mixed-symmetry states in  $^{134}\text{Xe}$  and  $^{136}\text{Ce}$  by measuring absolute transition strengths using the method of Coulomb excitation in inverse kinematics. Fig. 1.1 shows some of the nuclides in which mixed-symmetry states have been identified. First, it is important to positively identify mixed-symmetry states in the nuclei of interest if they exist. This will show the regions mixed-symmetry states exist and thus the regions where the description of nuclear states by the mixed-symmetry state description are valid. Second, if mixed-symmetry states are identified in these nuclides, one can study the systematics of these states with varying proton number along isotonic chains, namely for the  $N = 78$  and  $N = 80$  isotones. Studying the evolution of the properties of the mixed-symmetry states is an important step in constraining the parameters of the Interacting Boson Model, including the proton-neutron interaction.

### **Outline**

Finally, a brief outline of the remainder of this work will be given. In Chapter 2, some background on the Interacting Boson Model and mixed-symmetry states will be presented. The theory of Coulomb excitation, the method used for measuring transition strengths in the nuclei of interest, will be presented in Chapter 3. The details of the Coulomb excitation experiment, the methods of data analysis, and experimental results are given in Chapter 4. The evolution of the one-quadrupole phonon mixed-symmetry state in the  $N = 80$  and  $N = 78$  isotones based on the results is discussed in Chapter 5.

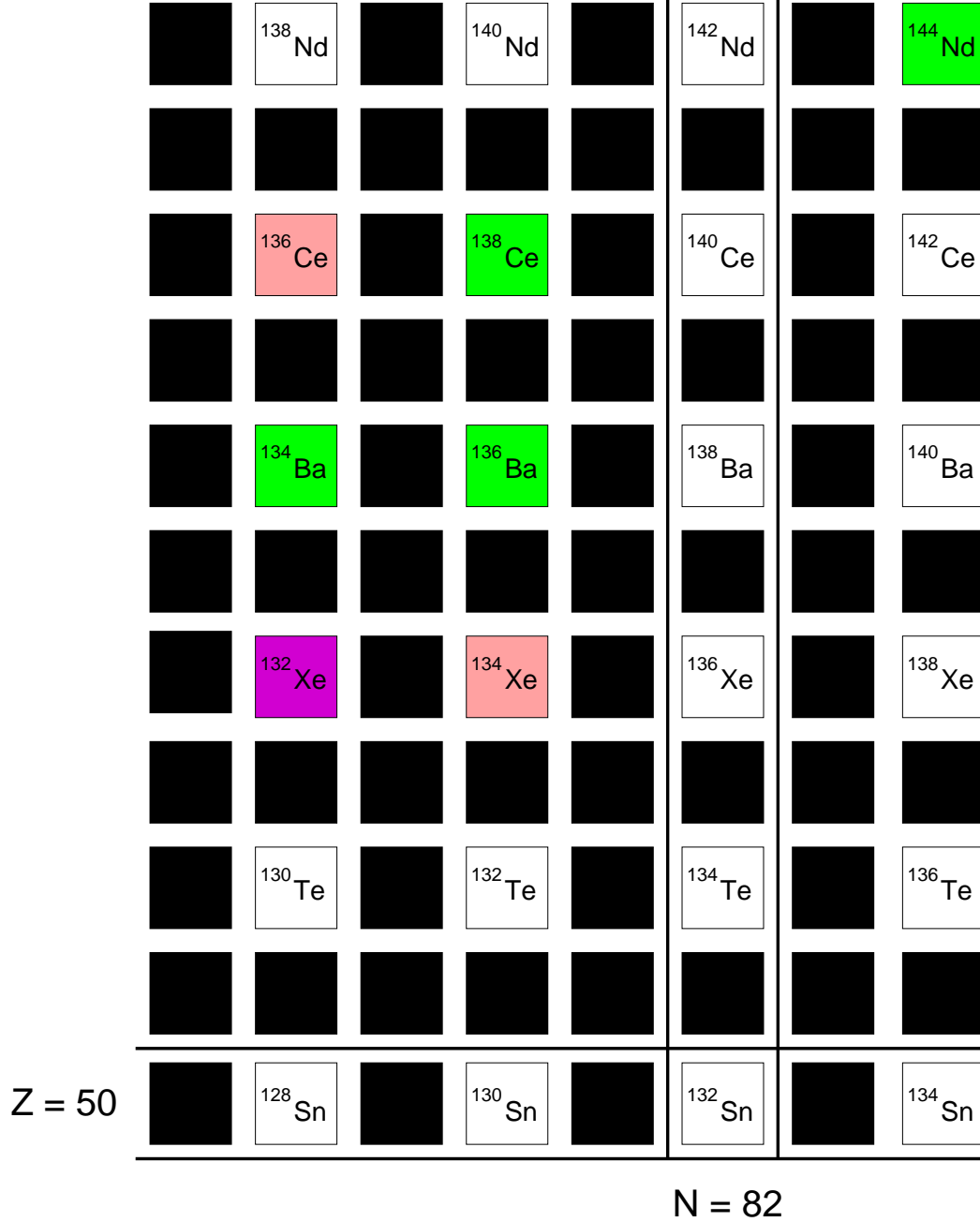


Figure 1.1: Nuclides in the  $A = 140$  mass region are shown. The green boxes indicate nuclides where mixed-symmetry states have been identified. The pink boxes indicate the nuclides studied in this present work. The magenta box indicates the nuclide where a mixed-symmetry state has been tentatively identified. The  $Z = 50$  and  $N = 82$  shell closures are indicated by lines.

## Chapter 2

# The Interacting Boson Model and Mixed-Symmetry States

The Interacting Boson Model (IBM) is a model for describing collective excitations in atomic nuclei. It has been introduced by Iachello and Arima in 1975 [15] and has been used to model a wide variety of nuclear properties and phenomena. One of the advantages of the model is its use of the symmetries of the boson operators introduced in the model, which allows for analytic expressions of the states and expectation values for three different ideal limits of nuclei. In this chapter a brief introduction and some background to the model will be presented. Most of the presentation of this chapter follows the book of Iachello and Arima [34].

### 2.1 Interacting Boson Model-1

In this section, the Interacting Boson Model-1 (IBM-1) will be introduced. Although the IBM-1 is not used explicitly in the analysis or direct interpretation of the present work, it is helpful to use it to formulate the basic ideas and expressions in the IBM and then extend it to the Interacting Boson Model-2 (IBM-2). In the IBM-1, the number of bosons is given by the number of pairs of protons and pairs of neutrons outside of closed shells. No distinction is made between proton type and neutron type bosons.

#### 2.1.1 Boson Creation and Annihilation Operators

The basic foundation of the Interacting Boson Model is that collective excitations can be described with bosons. These bosons can be of two types,  $s$  and  $d$  having and angular momentum of either  $L = 0$  or  $L = 2$  units of

$\hbar$ , respectively. Both bosons have positive parity. The number of bosons is determined by the number of nucleon pairs or hole pairs that are outside of a closed shell. The reason for this comes from the interpretation of the bosons as correlated nucleon pairs. The total number of bosons  $N$  in the IBM is a conserved quantity. In the IBM-1, the nucleon or hole pairs must be the same type of nucleon, meaning pairs consisting of a proton and neutron are not included. The IBM-1 is applicable only to even-even nuclei.

The nuclear states are represented in the framework of second quantization. The boson creation operators are given by  $s^\dagger$  and  $d_\mu^\dagger$  and the boson annihilation operators by  $s$  and  $d_\mu$ , where  $\mu = -2, -1, 0, 1, 2$ . They satisfy the following commutation relations:

$$\begin{aligned} [s, s] &= [s^\dagger, s^\dagger] = 0, \\ [s, d_\mu] &= [s^\dagger, d] = [s, d^\dagger] = [s^\dagger, d^\dagger] = 0, \\ [d_\mu, d_{\mu'}] &= [d_\mu^\dagger, d_{\mu'}^\dagger] = 0, \\ [d_\mu, d_{\mu'}] &= \delta_{\mu\mu'}. \end{aligned} \tag{2.1}$$

## Spherical Tensors

Since nuclear states studied in the laboratory almost always have a definite angular momentum, which results from the Hamiltonian being rotationally invariant, it is useful to use spherical tensors. These tensors transform as irreducible representations of the rotation group. Details about the properties of spherical tensors can be found in Appendix 1A of Ref. [35]. The boson creation operators transform as a spherical tensors while the spherical tensor for the annihilation operator needs to be defined as

$$\tilde{b}_{l,m} = (-)^{l+m} b_{l,-m}. \tag{2.2}$$

Two spherical tensors operators can be coupled as

$$T_m^{(l)} = [T^{(l_1)} \times T^{(l_2)}]_m^{(l)} \tag{2.3}$$

to form a new spherical tensor operator, where the product is defined as

$$[T^{(l_1)} \times T^{(l_2)}]_m^{(l)} = \sum_{m_1, m_2} \langle l_1 m_1 l_2 m_2 | l m \rangle T_{m_1}^{(l_1)} T_{m_2}^{(l_2)}, \tag{2.4}$$

where the symbol  $\langle l_1 m_1 l_2 m_2 | l m \rangle$  represents the Clebsch-Gordan coefficients. For example, to form a state with two bosons one would express it as

$$[b_{l,m}^\dagger \times b_{l',m'}^\dagger]_M^{(L)} |0\rangle, \tag{2.5}$$

where  $L$  and  $M$  are the angular momentum and magnetic quantum number of the state, respectively, whose values are restricted by the angular momentum addition rules.

A special case of the product of two tensor operators is the scalar product and the shorthand notation

$$U^{(l)} \cdot V^{(l)} = (-)^l (2l + 1)^{\frac{1}{2}} [U^{(l)} \times V^{(l)}]_0^{(0)}, \quad (2.6)$$

will be used.

## 2.1.2 Operators and Basis States

Operators in the IBM are constructed from the creation and annihilation operators. Since the total number of bosons is conserved, all the terms in an operator have the same number of creation and annihilation operators with the exception of pair transfer operators.

### Hamiltonian Operator

The Hamiltonian operator is given by the expression

$$H = E_0 + \sum_{\alpha, \beta} \epsilon_{\alpha\beta} b_{\alpha}^{\dagger} b_{\beta} + \sum_{\alpha, \beta, \delta, \gamma} \frac{1}{2} u_{\alpha\beta\gamma\delta} b_{\alpha}^{\dagger} b_{\beta}^{\dagger} b_{\delta} b_{\gamma} + \dots \quad (2.7)$$

The fact there are finite two-body and higher terms present shows that an interaction exists between bosons in a state and gives the Interacting Boson Model its name. A better way to express the Hamiltonian is to use spherical tensors coupled to definite angular momentum as

$$H = E_0 + \sum_l \epsilon_l b_l^{\dagger} \cdot \tilde{b}_l + \sum_{L, l, l', l''} [[b_l^{\dagger} \times b_{l'}^{\dagger}]^{(L)} \times [\tilde{b}_{l''} \times \tilde{b}_{l'''}]^{(L)}]_0^{(0)} + \dots \quad (2.8)$$

One can then see that the Hamiltonian is invariant under rotations.

Another useful way to express the Hamiltonian that is used in many practical applications of the IBM-1 is by using the multipole expansion

$$H = E'_0 + \epsilon_d \hat{n}_d + a_0 \hat{P}^{\dagger} \cdot \hat{P} + a_1 \hat{L} \cdot \hat{L} + a_2 \hat{Q} \cdot \hat{Q} + a_3 \hat{U} \cdot \hat{U} + a_4 \hat{V} \cdot \hat{V}, \quad (2.9)$$

where the multipole operators are given by

$$\begin{aligned}
\hat{n}_d &= d^\dagger \cdot \tilde{d} \\
\hat{P} &= \frac{1}{2} \tilde{d} \cdot \tilde{d} - \frac{1}{2} \tilde{s} \cdot \tilde{s} \\
\hat{L} &= 10^{\frac{1}{2}} [d^\dagger \times \tilde{d}]^{(1)} \\
\hat{Q} &= [d^\dagger \times \tilde{s} + s^\dagger \times \tilde{d}]^{(2)} - \frac{\sqrt{7}}{2} [d^\dagger \times \tilde{d}]^{(2)} \\
\hat{U} &= [d^\dagger \times \tilde{d}]^{(3)} \\
\hat{V} &= [d^\dagger \times \tilde{d}]^{(4)}.
\end{aligned} \tag{2.10}$$

With such a Hamiltonian, one is able to see more easily what the effect each multipole degree of freedom has on the nuclear states and determine which ones are the most important for a given set of nuclei.

### Basis states

Once the IBM-1 Hamiltonian is chosen, a basis of states needs to be chosen to find the corresponding energy eigenvalues and eigenstates. A basis may be constructed from states created by applying the boson creation operators to the vacuum state. This basis is represented as

$$B : b_\alpha^\dagger b_\beta^\dagger \dots |0\rangle. \tag{2.11}$$

To have states with definite angular momentum, the appropriate tensor product of boson creation operators can be used to give the set

$$B : [b_\alpha^\dagger \times b_\beta^\dagger \times \dots]_m^{(l)} |0\rangle. \tag{2.12}$$

It turns out that the angular momentum and magnetic quantum numbers are not sufficient to label all the states of a basis. Additional quantum numbers are needed to uniquely label the states. These additional quantum numbers can be found from the representations of a Lie algebra and its subalgebras that are formed from the bilinear products of creation and annihilation operators.

### Lie Algebras and Their Representations

The bilinear product of creation and annihilation operator  $b_\alpha^\dagger b_\beta$  are the elements of the unitary Lie algebra in six dimensions  $u(6)$ . There are 36 such pairs of operators and they are called the generators of the algebra. One may also take the tensor product of creation and annihilation operators to form

the same Lie algebra  $u(6)$  and in the IBM, these products will be used as the generators of the algebra.

The Lie algebra  $u(6)$  can be decomposed into a chain of subalgebras. If an appropriate chain of algebras can be found, the representations of each of these algebras can be used to label states with appropriate quantum numbers. This is because the states can be chosen that transform as the representations of each algebra. For applications to nuclei the chain of algebras must contain the subalgebra  $so(3)$  since it is needed for states to have as a representation of the rotation group. In other words,  $so(3)$  is required for states to have a good angular momentum quantum number. Three and only three chains of subalgebras have been found that contain the subalgebra  $so(3)$ . One of these chains is

$$\underbrace{u(6)}_N \supset \underbrace{u(5)}_{n_d} \supset \underbrace{so(5)}_{v, \bar{n}_\Delta} \supset \underbrace{so(3)}_L \supset \underbrace{so(2)}_M, \quad (2.13)$$

where under each algebra, the corresponding quantum number is given. Note that there are two quantum numbers given for the algebra  $so(5)$ . This is due to an ambiguity from reducing  $so(5)$  to  $so(3)$  and an additional quantum number is needed to uniquely specify the remaining representations. The quantum numbers  $L$  and  $M$  correspond to the angular momentum and magnetic quantum numbers.

Now basis states can be uniquely specified by using the quantum numbers that arise from one of the chains of algebras. For example, a basis built from the chain shown in Eq. (2.13) would be

$$B : [s^{\dagger n_s} d^{\dagger n_d}]_{v, \bar{n}_\Delta, L, M} |0\rangle, \quad (2.14)$$

where  $n_s$  is the number of  $s$  bosons. The total boson number is  $N = n_s + n_d$  and since this number is conserved, it reduces the number of independent parameters by one.

## Transition Operators

Once the eigenstates of a Hamiltonian are found, expectation values for transition operators can be calculated. The general form for the electromagnetic transition operator is given by

$$T^{(L)} = t_0^{(0)} \delta_{L0} + \sum_{\alpha, \beta} t_{\alpha\beta}^{(L)} b_\alpha^\dagger b_\beta + \dots, \quad (2.15)$$

where  $L$  is the multipole of the transition. Since all of the boson operators have positive parity, the all the transition operators also have positive par-

ity. States of nuclei have definite angular momentum and it is useful to use the spherical tensors coupled to definite angular momentum to construct the transition operators. The transition operators then become

$$T_{\mu}^{(L)} = t_0^{(0)} \delta_{L0} + \sum_{l'} t_{l'}^{(L)} [b_l^{\dagger} \times \tilde{b}_{l'}]_{\mu}^{(L)} + \dots \quad (2.16)$$

In terms of the multipole operators given in Eq. (2.10), the transition operators up to  $L = 4$  can be written as

$$\begin{aligned} T^{(E0)} &= \alpha_0 + \beta_0 \hat{n}_d, \\ T^{(M1)} &= \beta_1 \hat{L}, \\ T^{(E2)} &= \beta_1 \hat{Q} + \beta_1' \hat{Q}', \\ T^{(M3)} &= \beta_3 \hat{U}, \\ T^{(E4)} &= \beta_4 \hat{V}, \end{aligned} \quad (2.17)$$

where  $\alpha_0$  and  $\beta_L$  are parameters and  $\hat{Q}'$  is given by

$$\hat{Q}' = [d^{\dagger} \times d^{\dagger}]^{(2)}. \quad (2.18)$$

Eq. (2.17) is a useful and intuitive form for the transition operators and they will be extended to include the different boson types in the Interacting Boson Model-2.

## 2.2 Interacting Boson Model-2

In the Interacting Boson Model-2 (IBM-2), the model is extended by differentiating between proton type bosons and neutron type bosons [17, 36]. Each are interpreted as a correlated pair of valence protons and neutrons, respectively. Each boson operator now has an additional label denoting whether it is a proton or neutron boson. They follow the following commutation relations:

$$\begin{aligned} [b_{\rho,l,m}, b_{\rho',l',m'}^{\dagger}] &= \delta_{\rho\rho'} \delta_{ll'} \delta_{mm'}, \\ [b_{\rho,l,m}, b_{\rho',l',m'}] &= 0, \\ [b_{\rho,l,m}^{\dagger}, b_{\rho',l',m'}^{\dagger}] &= 0, \end{aligned} \quad (2.19)$$

where  $b_{\rho,l,m}$  and  $b_{\rho,l,m}^{\dagger}$  are the boson annihilation and creation operators, respectively, and  $\rho$  is the proton or neutron label,  $l$  is the angular momentum quantum number of the boson, and  $m$  is the magnetic quantum number of the boson.



## IBM-2 Hamiltonian

The IBM-2 Hamiltonian can be written as a sum of three terms,

$$H = H_\pi + H_\nu + V_{\pi\nu}. \quad (2.20)$$

Using coupled spherical tensors, the terms  $H_\pi$  and  $H_\nu$  are given by

$$H_\rho = E_0^\rho + \sum_l \epsilon_l^\rho b_{\rho l}^\dagger \cdot \tilde{b}_{\rho l} + \sum_{L,l,l',l''} \frac{1}{2} u_{ll'l''}^{\rho L} [[b_{\rho l}^\dagger \times b_{\rho l'}^\dagger]^{(L)} \times [\tilde{b}_{\rho l''} \times \tilde{b}_{\rho l'''}]^{(L)}]_0^{(0)} + \dots, \quad (2.21)$$

which has exactly the same form as Eq. (2.8), the only difference being the use of only either proton or neutron bosons operators. The difference between the IBM-1 and IBM-2 Hamiltonians is due to the presence of the third term  $V_{\pi\nu}$  in Eq. (2.20), which is given by

$$V_{\pi\nu} = \sum_{\alpha\beta\gamma\delta} w_{\alpha\beta\gamma\delta} b_{\pi\alpha}^\dagger b_{\pi\beta} b_{\nu\gamma}^\dagger b_{\nu\delta} + \dots \quad (2.22)$$

This term contains two-body terms that have both proton and neutron creation and annihilation operators, but in a way that conserves the number of protons and neutrons. This is a requirement for the Hamiltonian since the bosons are interpreted as nucleon pairs and the number of each nucleon must be a constant. The expression for  $V_{\pi\nu}$  with coupled spherical tensors is

$$V_{\pi\nu} = \sum_{L,l,l',l''} w_{l,l',l''}^L [[b_{\pi l}^\dagger \times \tilde{b}_{\pi l'}]^{(L)} \times [b_{\nu l''}^\dagger \times \tilde{b}_{\nu l'''}]^{(L)}]_0^{(0)} + \dots, \quad (2.23)$$

which is obtained in the standard way using the tensor product.

The IBM-2 Hamiltonian can also be expressed using a multipole expansion. The terms  $H_\pi$  and  $H_\nu$  takes the same form as the multipole expanded IBM-1 Hamiltonian given by Eq. (2.9) with the boson operators being labelled appropriately for either proton or neutron operators. The multipole operators are also given by Eq. (2.10) with the appropriate proton and neutron boson operator labels. For example, the quadrupole operator is given by

$$\hat{Q}_\rho = [d_\rho^\dagger \times \tilde{s}_\rho + s_\rho^\dagger \times \tilde{d}_\rho]^{(2)} - \frac{\sqrt{7}}{2} [d_\rho^\dagger \times \tilde{d}_\rho]^{(2)}. \quad (2.24)$$

Along with the additional quadrupole terms

$$\hat{Q}'_\rho = [d_\rho^\dagger \times \tilde{d}_\rho]^{(2)} \quad (2.25)$$

$$\hat{Q}''_\rho = i[d_\rho^\dagger \times \tilde{s}_\rho - s^\dagger \times \tilde{d}_\rho]^{(2)}, \quad (2.26)$$

the multipole expansion of  $V_{\pi\nu}$  is given as

$$\begin{aligned} V_{\pi\nu} = & c_0 \hat{n}_{d_\pi} \cdot \hat{n}_{d_\nu} + c_1 \hat{L}_\pi \cdot \hat{L}_\nu \\ & + c_2 \hat{Q}_\pi \cdot \hat{Q}_\nu + c'_2 \hat{Q}_\pi \cdot \hat{Q}'_\nu + c''_2 \hat{Q}'_\pi \cdot \hat{Q}_\nu + c'''_2 \hat{Q}'_\pi \cdot \hat{Q}'_\nu + c_2^{iv} \hat{Q}''_\pi \cdot \hat{Q}''_\nu \\ & + c_3 \hat{U}_\pi \cdot \hat{U}_\nu + c_4 \hat{V}_\pi \cdot \hat{V}_\nu. \end{aligned} \quad (2.27)$$

The term  $V_{\pi\nu}$  is important because it quantifies the interaction between proton and neutron degrees of freedom.

### IBM-2 Basis states

As it was mentioned in Section 2.1.2, basis states can be found by choosing states that transform as the representations of the chain of algebras that can be derived from the  $u(6)$  algebra formed by the bilinear pair of boson creation and annihilation operators. In the IBM-2, the bilinear pairs of proton and neutron creation and annihilation operators respectively form the algebras  $u_\pi(6)$  and  $u_\nu(6)$ . There are several ways decompose and combine the two algebras into a chain of subalgebras and each way will determine the basis. As in the IBM-1, the requirement for the chain is the inclusion of the  $so_{\pi+\nu}(3)$  algebra as it is related to a good total angular momentum quantum number. The algebra  $so_{\pi+\nu}(3)$  is created from the sum of generators of the algebras  $so_\pi(3)$  and  $so_\nu(3)$ .

As an example, one may take the two chains of algebras for protons and neutron,

$$\begin{aligned} u_\pi(6) \supset u_\pi(5) \supset so_\pi(5) \supset so_\pi(3) \supset so_\pi(2) \\ u_\nu(6) \supset u_\nu(5) \supset so_\nu(5) \supset so_\nu(3) \supset so_\nu(2). \end{aligned} \quad (2.28)$$

These two chains can be combined at any point up except at  $so_{\pi+\nu}(2)$  since

the combined algebra  $so_{\pi+\nu}(3)$  is needed. One of the possibilities is

$$\begin{array}{c}
 \underbrace{u_{\pi}(6)}_{N_{\pi}} \supset \underbrace{u_{\pi}(5)}_{n_{d\pi}} \supset \underbrace{so_{\pi}(5)}_{v_{\pi}, n_{\pi\Delta}} \supset \underbrace{so_{\pi}(3)}_{L_{\pi}} \searrow \\
 \underbrace{so_{\pi+\nu}(3)}_L \supset \underbrace{so_{\pi+\nu}(2)}_M, \quad (2.29) \\
 \underbrace{u_{\nu}(6)}_{N_{\nu}} \supset \underbrace{u_{\nu}(5)}_{n_{d\nu}} \supset \underbrace{so_{\nu}(5)}_{v_{\nu}, n_{\nu\Delta}} \supset \underbrace{so_{\nu}(3)}_{L_{\nu}} \nearrow
 \end{array}$$

where the quantum numbers are labelled beneath the corresponding algebra. This is the basis that is used in the IBM-2 program NPBOS.

Another set of bases can be obtained if one combines the algebras at a different point such as

$$\begin{array}{c}
 u_{\pi}(6) \searrow \\
 u_{\pi+\nu}(6) \supset u_{\pi+\nu}(5) \supset so_{\pi+\nu}(5) \supset so_{\pi+\nu}(3) \supset so_{\pi+\nu}(2), \quad (2.30) \\
 u_{\nu}(6) \nearrow
 \end{array}$$

where we have again used the chains in Eq. (2.28). In general there are three chains that can be combined at  $u_{\pi+\nu}(6)$  to give three different bases. In these chains, the proton and neutron bosons exhibit a symmetry and this is the subject of the following section.

### 2.2.1 Full and Mixed Proton Neutron Symmetry

In the IBM-1, the total boson state has to be symmetric under the interchange of any two bosons of the state. A convenient way to represent the permutation symmetry of an object is to use the Young diagram, whose description can be found in Appendix 1C of Ref. [35]. Completely symmetric states are represented by a Young diagram which has boxes aligned only horizontally, whereas completely anti-symmetric states are represented by boxes aligned vertically. States with that are neither completely symmetric nor anti-symmetric have mixed symmetry and are represented by Young diagrams that have neither completely horizontally nor completely vertically aligned boxes. The completely symmetric boson states in the IBM-1 are represented by the diagram

$$\overbrace{\boxed{\phantom{0}} \boxed{\phantom{0}} \cdots \boxed{\phantom{0}}}^N, \quad (2.31)$$

or represented by  $[N]$ , called the partition, where  $N$  is the total number of bosons in a state. In general the number  $\lambda_n$  of the partition  $[\lambda_1, \lambda_2, \dots, \lambda_n]$

represents the number of boxes in the  $n$ -th row of the corresponding Young diagram.

In the IBM-2, one can take the direct product of the algebras  $u_\pi(6) \otimes u_\nu(6)$  to form the algebra for the whole system. Using the representations of each algebra, the Kronecker product can be taken to form the representation of the combined algebra. This new representation can be decomposed into a direct sum of a symmetric and mixed-symmetry representations as given by

$$[N_\pi] \otimes [N_\nu] = \bigoplus_{k=0}^P [N_\pi + N_\nu - k, k], \quad (2.32)$$

where

$$P = \begin{cases} N_\pi & \text{for } N_\pi \leq N_\nu \\ N_\nu & \text{for } N_\nu \leq N_\pi. \end{cases} \quad (2.33)$$

The term in the direct sum with  $k = 0$  corresponds to the fully-symmetric representation and the remaining terms correspond to the mixed-symmetry representations. The Young diagrams for the mixed-symmetry representations each have exactly two rows. It is from the product in Eq. (2.32) that mixed-symmetry representations arise from two representations that are completely symmetric. The resulting representations can be used as the basis states for the two particle system.

A simple example will be shown to illustrate the representations obtained from Eq. (2.32). For  $N_\pi = N_\nu = 1$ , the product of the representations are

$$[1] \otimes [1] = [2] \oplus [1, 1], \quad (2.34)$$

which can be represented by Young diagrams as

$$\square \otimes \square = \square \square \oplus \begin{array}{|c|} \hline \square \\ \hline \square \\ \hline \end{array}. \quad (2.35)$$

In this case of only one proton boson and one neutron boson, the Kronecker product of the representations results in a completely symmetric state and completely anti-symmetric state. In general, for  $N_\rho > 1$  for one type of boson and  $N_{\rho'} \geq 1$  for the other type will result in states with mixed-symmetry.

## ***F* spin**

The use of the partitions and Young diagrams above to quantify the symmetry of the boson operators is general and applicable to any system with permutation symmetry. This is useful because many analogies can be made to systems that exhibit or approximately exhibit the same type of symme-

try. One example is the concept of isospin, sometimes called isobaric spin, where protons and neutrons are considered the same particle that can be in two different states. This symmetry between proton and neutron is rooted in the charge independence of the nucleon-nucleon interaction along with the fact that the electromagnetic interaction is small in magnitude compared to it. The reason that this approximate symmetry is so useful is that it exhibits exactly the same symmetry as a spin  $\frac{1}{2}$  particle and therefore all the tools used in angular momentum algebra can be used to derive results based on the approximate symmetry between proton and neutron. The concept of  $F$  spin [17] extends the concept of isospin to the proton and neutron bosons of the IBM-2. The value of  $F$  spin for a proton boson and neutron boson is given by

$$b_{\pi}^{\dagger} |0\rangle = \begin{cases} F = \frac{1}{2} \\ F_z = +\frac{1}{2} \end{cases} \quad (2.36)$$

$$b_{\nu}^{\dagger} |0\rangle = \begin{cases} F = \frac{1}{2} \\ F_z = -\frac{1}{2} \end{cases}. \quad (2.37)$$

The total  $F$  spin of a state is given by



$$F = \frac{N_{\pi} + N_{\nu} - k}{2}, \quad (2.38)$$

where  $k$  is the index used to characterize the representations in Eq. (2.32) and the total  $F$  spin projection  $F_z$  is given by

$$F_z = \frac{N_{\pi} - N_{\nu}}{2}. \quad (2.39)$$

The nuclear basis states can be labelled with  $F$  and  $F_z$  for a given total boson number  $N$  to specify the type of proton-neutron symmetry it has. Though the proton-neutron symmetry of the bosons in the IBM-2 can be represented with partitions and Young diagrams as was shown, the familiarity of many with angular momentum algebra makes  $F$  spin a useful and intuitive concept.

To fully specify the basis states resulting from the  $u_{\pi}(6) \times u_{\nu}(6) \supset u_{\pi+\nu}(6)$  algebra chain, also called the  $F$ -spin basis, the quantum numbers that result from the remaining chain of subalgebras are needed. As was noted earlier, there are three possible chains, namely the ones containing the  $u_{\pi+\nu}(5)$ ,  $su_{\pi+\nu}(3)$ , and  $so_{\pi+\nu}(6)$  algebras. A detailed derivation of such quantum numbers are outlined in Chapter 5 of the book of Iachello and Arima [34]. Once all the quantum numbers are specified, one has a complete basis with which to work

<p>[2]</p>  <p><math>F = 1</math></p>	<p>[1,1]</p>  <p><math>F = 0</math></p>
$[d_\pi^\dagger \times d_\nu^\dagger]^{(0),(2),(4)}  0\rangle$	$\underline{0^+} \underline{2^+} \underline{4^+}$
$\frac{1}{\sqrt{2}}[d_\pi^\dagger \times s_\nu^\dagger + d_\nu^\dagger \times s_\pi^\dagger]^{(2)}  0\rangle$	$\underline{2^+}$
$[s_\pi^\dagger \times s_\nu^\dagger]^{(0)}  0\rangle$	$\underline{0^+}$

	<p><math>\underline{1^+} \underline{3^+}</math> <math>[d_\pi^\dagger \times d_\nu^\dagger]^{(1),(3)}  0\rangle</math></p> <p><math>\underline{2^+}</math> <math>\frac{1}{\sqrt{2}}[d_\pi^\dagger \times s_\nu^\dagger - d_\nu^\dagger \times s_\pi^\dagger]^{(2)}  0\rangle</math></p>
--	--

Figure 2.1: Example of IBM-2 states in  $u(5)$  limit. Building blocks of collective excitations.

with.

Here only an example will be given for basis states of the chain of algebras containing  $u_{\pi+\nu}(5)$ , often called simply the  $u(5)$  limit to illustrate the concept of  $F$  spin. Shown in Fig. 2.1 is a set of nuclear states in the  $u(5)$  limit for a nucleus with  $N_\pi = 1$  and  $N_\nu = 1$ . The states are labelled by the appropriate  $s$  and  $d$  boson operators. The states on the left correspond to the fully-symmetric states and the states on the right correspond to mixed-symmetry states. It can be seen that the pairwise exchange of proton and neutron labels produce the same state for the fully-symmetric states and the same state with a factor  $-1$  for the mixed-symmetry states. The reason the exchange of proton and neutron labels are limited to pairwise exchange is because the individual proton and neutron numbers need to be conserved.

### Geometric Interpretation

In the IBM-1, geometrical shapes can be assigned to the algebras of the three possible chains, which correspond directly to the description of nuclear

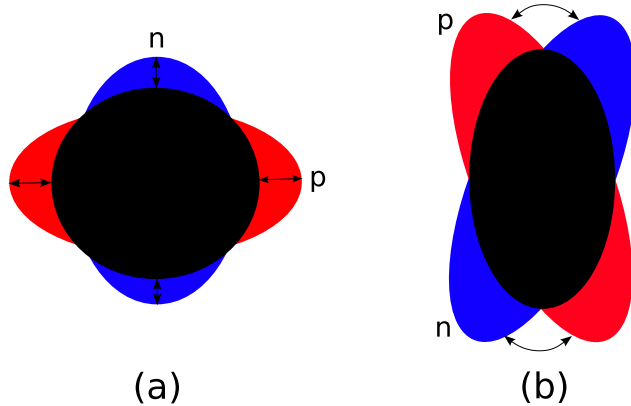


Figure 2.2: Geometric interpretation of mixed-symmetry states are shown. The figure represents a snapshot of the nucleus in time where the red indicates the proton fluid and the blue represents the neutron fluid. Part (a) represents the out of phase vibration for spherical nuclei and (b) represents the vibration of protons and neutrons with respect to each other for prolate or oblate deformed nuclei.

shapes by Bohr and Mottlesohn's shape variables [11, 12]. In the IBM-2, the mixed-symmetry states correspond to a quadrupole vibration where the protons and neutrons oscillate out of phase as shown in part (a) of Fig. 2.2. For deformed nuclei, the protons and neutrons oscillate with respect to one another as the nucleus as a whole rotates as shown in part (b) of Fig. 2.2. Because of this type of motion, the mixed-symmetry states for deformed nuclei are also known as the scissors mode.

### 2.2.2 Signature of Mixed-Symmetry States

Mixed-symmetry states can be identified by their unique signature, namely a collective  $M1$  decay to a fully-symmetric state.  $M1$  transitions are forbidden between fully-symmetric states and between mixed-symmetry states in the  $F$ -spin basis.

#### IBM-2 Transition Operators

$$T^{(L)} = T_{\pi}^{(L)} + T_{\nu}^{(L)} \quad (2.40)$$

$$T_{\rho\mu}^{(L)} = t_{\rho 0}^{(0)} \delta_{L0} + \sum_{l'} t_{\rho l'}^{(L)} [b_{\rho l}^\dagger \times \tilde{b}_{\rho l'}]_{\mu}^{(L)} + \dots \quad (2.41)$$

In the IBM-2, multipole transition operators have the form that is an extension of the IBM-1 operators. The magnetic transition operators are given by

$$T^{(M1)} = \sqrt{\frac{3}{4\pi}} (g_{\pi} \hat{L}_{\pi} + g_{\nu} \hat{L}_{\nu}) \quad (2.42)$$

$$T^{(M3)} = \sqrt{\frac{7}{4\pi}} (m_{\pi} \hat{U}_{\pi} + m_{\nu} \hat{U}_{\nu}), \quad (2.43)$$

where the coefficients in front of the multipole operators are the effective proton and neutron boson moments, respectively. The electric transition operators are given by

$$T^{(E2)} = e_{\pi} \hat{Q}_{\pi}^{\chi} + e_{\nu} \hat{Q}_{\nu}^{\chi}, \quad (2.44)$$

$$T^{(E4)} = t_{\pi} \hat{V}_{\pi} + t_{\nu} \hat{V}_{\nu}, \quad (2.45)$$

where

$$\hat{Q}_{\rho}^{\chi} = [d_{\rho}^{\dagger} \times \tilde{s}_{\rho} + s_{\rho}^{\dagger} \times \tilde{d}_{\rho}]^{(2)} + \chi_{\rho} [d_{\rho}^{\dagger} \times \tilde{d}_{\rho}]^{(2)}. \quad (2.46)$$

The coefficients in front of the multipole operators are the proton and neutron boson effective charges respectively. For our experiment, only  $M1$  and  $E2$  transitions will be significant.

### Decay of the $2_{1,\text{ms}}^{+}$ State

In the limit of  $u_{\pi+\nu}(5)$ , the Hamiltonian is diagonal in the  $u_{\pi+\nu}(5)$   $F$ -spin basis and the transition matrix elements connecting the states can be calculated analytically. We are especially interested in the decay of the one-phonon  $2_{1,\text{ms}}^{+}$  mixed-symmetry state. The  $M1$  transition matrix element is given by

$$\langle 2_1^{+} || T^{(M1)} || 2_{1,\text{ms}}^{+} \rangle = \sqrt{\frac{3}{4\pi}} \sqrt{\frac{30N_{\pi}N_{\nu}}{N^2}} (g_{\pi} - g_{\nu}) \quad (2.47)$$

and the  $E2$  transition matrix elements are given by

$$\langle 0_1^{+} || T^{(E2)} || 2_{1,\text{ms}}^{+} \rangle = \sqrt{\frac{2N_{\pi}N_{\nu}}{N}} (e_{\nu} - e_{\pi}) \quad (2.48)$$

$$\langle 2_1^{+} || T^{(E2)} || 2_{1,\text{ms}}^{+} \rangle = \sqrt{\frac{5N_{\pi}N_{\nu}}{N^2}} (e_{\nu}\chi_{\nu} - e_{\pi}\chi_{\pi}). \quad (2.49)$$



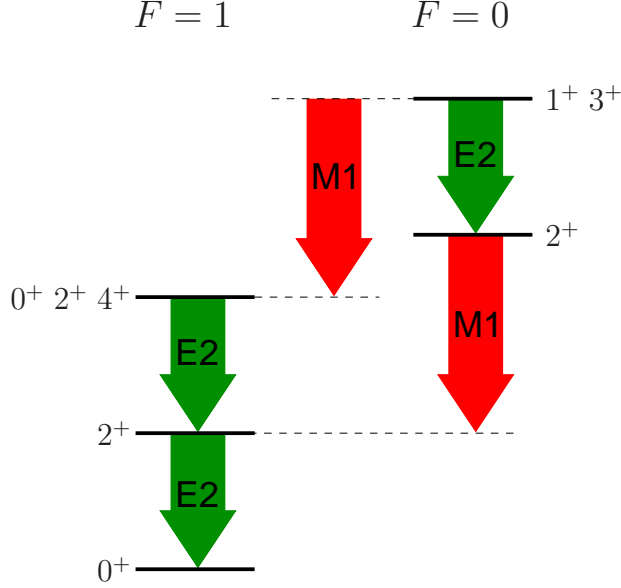


Figure 2.3: Figure showing the signature  $M1$  decays of mixed-symmetry states.

For boson  $g$  factors of  $g_\pi \approx 1\mu_N$  and  $g_\nu \approx 0$ , the  $M1$  transition matrix element is finite for the  $2_{1,ms}^+$  state. As it was mentioned earlier,  $M1$  transitions are forbidden between fully-symmetric states and also between mixed-symmetry states. Since, no other  $M1$  transitions are allowed except for the one connecting a mixed-symmetry state to a fully-symmetric state, it is used as the unique signature of a mixed-symmetry state. The  $E2$  transition between the  $2_{1,ms}^+$  and the  $0_1^+$  ground state is small assuming  $e_\pi \approx e_\nu$ , whereas  $E2$  transitions are large between fully-symmetric states and between mixed-symmetry states. The decay of the states in the  $u_{\pi+\nu}(5)$  limit is illustrated in Fig. 2.3.

A rough estimate for the  $M1$  transition strength for the decay of the one-phonon  $2_{1,ms}^+$  state can be obtained by taking the boson  $g$  factors to be  $g_\pi \approx 1$  and  $g_\nu \approx 0$ . Using Eq. (2.42), one obtains  $\langle 2_1^+ || T^{(M1)} || 2_{1,ms}^+ \rangle \approx 1 \mu_N$ , which usually results in short lifetime for the  $2_{1,ms}^+$  state, making it difficult to measure the transition strength. One way is through the use of Coulomb excitation, the theory of which will be discussed in the next chapter.

# Chapter 3

## Coulomb Excitation

Coulomb excitation is the process by which a nucleus is excited via the interaction of the Coulomb field with another charged particle. Though the process of exciting nuclear from inelastic scattering due to the electromagnetic interaction was first proposed in the 1920's and 1930's, it was in the early 1950's that Coulomb excitation started to be studied and used extensively<sup>1</sup>. Since then, the theory of Coulomb excitation has been well developed and its exposition can be found in several books and review articles [37–40]. Coulomb excitation is well suited for studying nuclear states because the process proceeds via the electromagnetic interaction, which is very well understood, as opposed to the nucleon-nucleon interaction, which is not known as well. It also populates collective nuclear states relatively strongly, which makes Coulomb excitation a well suited tool for studying collective excitations.

The Coulomb excitation cross sections are directly related to the transition matrix elements for electromagnetic decay and thus the transition matrix elements can be measured from the measurement of Coulomb excitation cross sections. Most of these matrix elements are for electric as opposed to magnetic decay as the probability for magnetic excitation is relatively small. The theory of Coulomb excitation also allows one to calculate the angular distribution of  $\gamma$  rays emitted from a Coulomb excited state. By measuring the angular distribution  $\gamma$  rays, the multipole mixing ratio of transitions of mixed multipolarity can be measured. Both electric transition matrix elements and multipole mixing ratios are needed to measure absolute  $M1$  transition strengths, which are needed for the identification of mixed-symmetry states.

In the following chapter, some of the of the theory of Coulomb excitation will be presented that is relevant for our experiments. The results will be used later in Chapter 4 when programs are used to calculate Coulomb excita-

---

<sup>1</sup>See Chapter 1 of Biedenharn and Brussaard [37] for a brief historical account

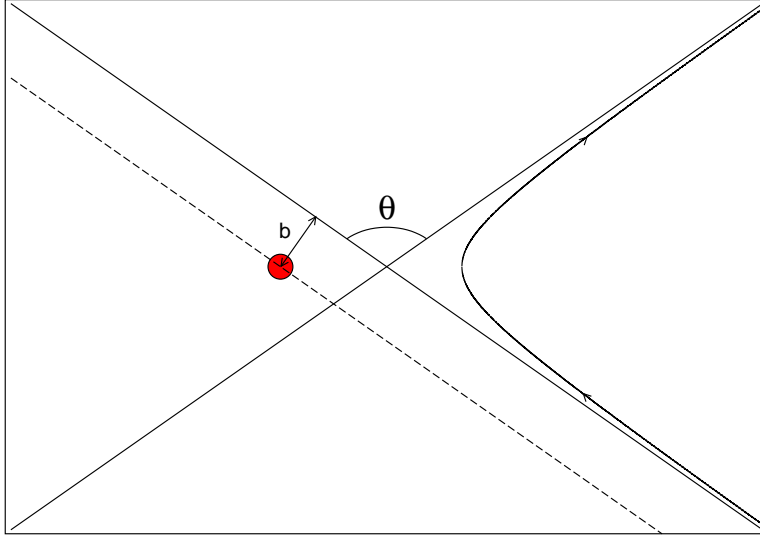


Figure 3.1: The scattering of the projectile off the target is shown. Classically for elastic scattering, the path of the projectile is a hyperbola where  $\theta$  is the scattering angle and  $b$  is the impact parameter.

tion cross sections and angular distribution coefficients. Most of the material presented in this chapter and further details can be found in Refs. [39, 41, 42].

### 3.1 Semi-Classical Theory

The semi-classical theory of Coulomb excitation has been extensively developed. The projectile is considered to move in a classical trajectory, deflected by the Coulomb force due to the electric field of the target. This trajectory, shown in Fig. 3.1, is the well known hyperbola for the elastic scattering of charged particles. The use of a semi-classical theory is justified when the distance of closest approach of the target and projectile nuclei is significantly larger than their de Broglie wavelengths. This ratio of the distance of closest approach to the wavelength of the nuclei is represented by the dimensionless quantity  $\eta$ , sometimes called the Sommerfeld parameter. It is defined as

$$\eta = 2\pi \frac{a}{\lambda} = \frac{Z_1 Z_2 e^2}{\hbar v}, \quad (3.1)$$

where  $a$  is half the distance of closest approach,  $\lambda$  is the de Broglie wavelength of the nucleus of interest,  $Z_1$  is the atomic number of the projectile,  $Z_2$  is the

atomic number of the target, and  $v$  is the (velocity of the projectile). All of the quantities are expressed in cgs units. The half the distance of closest approach is given by

$$a = \frac{Z_1 Z_2 e^2}{M_0 v^2}, \quad (3.2)$$

where  $Z_1$ ,  $Z_2$ , are the charges of the projectile nucleus and target nucleus, respectively,  $e$  is the charge of the electron,  $M_0$  is the reduced mass, and  $v$  is the initial velocity of the projectile. The condition for using the classical approximation is  $\eta \gg 1$ .

Another important parameter in Coulomb excitation is the adiabacity parameter  $\xi$ , which is defined as

$$\xi = \frac{a}{\hbar v} \Delta E, \quad (3.3)$$

where  $\Delta E$  is the excitation energy of the excited nuclear state. The parameter  $\xi$  gives the ratio between the nuclear state's oscillation period and the collision time. The collision time must be smaller than the nuclear period in order to substantially excite the state. As the value of  $\xi$  becomes large, the collision process becomes adiabatic and the probability to excite the state falls dramatically. In the other limit where  $\xi \rightarrow 0$ , the excitation process can be analyzed using the so called sudden approximation.

## Coupled Differential Equations

When the cross section for exciting a state is small compared to the elastic scattering cross section, first-order time-dependent perturbation theory can be used to calculate Coulomb excitation amplitudes where the perturbing potential is the changing electromagnetic field as the projectile and target nuclei pass each other. This approach is not sufficient to describe the situation when there are multiple excitations. For this situation, finding the excitation amplitudes from the solutions of the coupled set of differential equations governing the excitation process is needed. Outlined below is the theory that is the basis for the coupled-channel programs that are used in the analysis of the experimental data.

The excitation process is described by the time-dependent Schrödinger equation,

$$i\hbar \frac{\partial}{\partial t} |\psi\rangle = (H_0 + H_E(t)) |\psi\rangle, \quad (3.4)$$

where  $|\psi\rangle$  is the time-dependent state,  $H_0$  is the free nucleus Hamiltonian, and  $H_E(t)$  is the time-dependent Hamiltonian that arises from the changing elec-

tromagnetic field. To transform the Schrödinger equation to a set of coupled differential equations, the state vector  $|\phi\rangle$  is introduced as

$$|\psi\rangle = e^{i-H_0t/\hbar}|\phi\rangle. \quad (3.5)$$

This state vector is independent of time before and after the collision and satisfies

$$i\hbar\frac{\partial}{\partial t}|\phi\rangle = e^{iH_0t/\hbar}H_E(t)e^{-iH_0t/\hbar}|\phi\rangle. \quad (3.6)$$

Using the eigenstates  $|n\rangle$  of  $H_0$

$$H_0|n\rangle = E_n|n\rangle, \quad (3.7)$$

we define the time-dependent amplitude

$$a_n(t) = \langle n|\phi\rangle = \langle n|\psi\rangle e^{iE_nt/\hbar}. \quad (3.8)$$

Multiplying Eq. (3.9) by  $\langle n|$  and using the closure relation  $\sum_m|m\rangle\langle m| = 1$  results in the coupled differential equation

$$\dot{a}_n(t) = \sum_m \langle n|H_E(t)|m\rangle e^{i(E_n-E_m)t/\hbar}a_m(t). \quad (3.9)$$

Here  $H_E(t)$  is given by

$$H_E(t) = \sum_{\lambda,\mu} \frac{4\pi Z_1 e}{2\lambda+1} r_p^{-\lambda-1}(t) Y_{\lambda\mu}[\theta(t), \phi(t)] \mathcal{M}^*(E\lambda, \mu), \quad (3.10)$$

where  $r_p$  is distance of the particle from the origin,  $Y_{\lambda\mu}[\theta(t), \phi(t)]$  are the spherical harmonics and  $\mathcal{M}(E\lambda, \mu)$  is the electric multipole operator given by

$$\mathcal{M}(E\lambda, \mu) = \int r^\lambda \rho(\mathbf{r}) Y_{\lambda\mu}(\theta, \phi) d^3r \quad (3.11)$$

where  $\rho(\mathbf{r})$  is the nuclear charge density. It is through  $\langle n|H_E(t)|m\rangle$  the transition matrix elements enter the differential equations.

The initial conditions that have to be satisfied by the differential equations are

$$a_n(-\infty) = \delta_{0n}, \quad (3.12)$$

where  $\delta_{0n}$  is the Kronecker delta. This means the nucleus is in the ground state before the collision. The amplitude of excitation to a state is given by the value  $a_n = a_n(\infty)$ . Implicit is the assumption that the excitation process

and subsequent radiative decay are sufficiently separated in time. For decays such as particle emission that have very short lifetimes, this assumption may not be valid and the effect of the decay on the excitation process has to be taken into account.

The amplitudes for the states  $n$  can be found by numerically integrating Eq. (3.9). This method is used to calculate Coulomb excitation cross sections by several commonly used programs including CLX [43, 44], the program used for the analysis of our data. Directly integrating Eq. (3.9) has the advantage of being completely general in two ways. First, it does not need to make use of a specific nuclear model such as the vibrational or rotational model. Second, it also includes the effects of multistep excitations, which are not included in a first-order perturbation treatment.

### 3.1.1 Coulomb Excitation Cross Sections

Once the amplitudes for Coulomb excitation are obtained, whether it is from first-order perturbation theory or the integration of the coupled differential equations mentioned in the previous section, they can be used to calculate the Coulomb excitation cross section. The probability for excitation is given by

$$P_n = \frac{1}{2J_1 + 1} \sum_{M_1, M_n} |a_{I_n M_n}(M_1)|^2, \quad (3.13)$$

where  $a_{I_n M_n}(M_1)$  is the amplitude for excitation to state  $n$  with angular momentum and magnetic quantum numbers  $I_n$  and  $M_n$ , respectively, and  $M_1$  is the magnetic quantum number of the initial state. The total probability must be equal to unity,

$$\sum_n P_n = 1. \quad (3.14)$$

The Rutherford cross section, which gives the differential cross section for elastic scattering, is

$$\left(\frac{d\sigma}{d\Omega}\right)_{\text{Ruth}} = \frac{a^2}{4 \sin^4\left(\frac{\theta}{2}\right)}, \quad (3.15)$$

where  $a$  is half the distance of closest approach as given by Eq. (3.2). The differential cross section for Coulomb excitation is given by the product of the excitation probability  $P_n$  and the Rutherford cross section as given by

$$\frac{d\sigma_n}{d\Omega} = P_n \left(\frac{d\sigma}{d\Omega}\right)_{\text{Ruth}} = P_n \frac{a^2}{4 \sin^4\left(\frac{\theta}{2}\right)}. \quad (3.16)$$

The total cross section for excitation to state  $n$  is obtained by simply integrat-

ing over the whole solid angle,

$$\sigma_n = \frac{a^2}{4} \int_S P_n(\theta) \frac{d\Omega}{\sin^4(\frac{\theta}{2})} = a^2 \pi \int_0^\pi P_n(\theta) \frac{\cos(\frac{\theta}{2})}{\sin^3(\frac{\theta}{2})} d\theta. \quad (3.17)$$

### Symmeterization of Cross Sections

One of the deficiencies of the semi-classical treatment of the scattering process is the point along the path of the projectile at which the excitation of the nucleus takes place is unknown and this necessarily perturbs the orbit of the projectile. In order to compensate for this effect, one can use symmetrized parameters for the cross sections, which is roughly an averaging between initial and final parameters of the orbits. The symmeterized adiabacity parameter is given by

$$\xi_s = \frac{Z_1 Z_2 e^2}{\hbar \left( \frac{1}{v_f} - \frac{1}{v_i} \right)}, \quad (3.18)$$

where  $v_i$  and  $v_f$  are the initial and final velocities, respectively. The symmetrized value for half the distance of closest approach is given by

$$a_s = \frac{Z_1 Z_2 e^2}{M_0 v_f v_i}. \quad (3.19)$$

The expressions given in Eqs. (3.18) and (3.19) are used for one-step Coulomb excitation, but use of the expressions for multiple Coulomb excitation will in general violate the conservation of probability given in Eq. (3.14). A slightly different method is used to symmeterize the parameters that are used in the program of Winther and De Boer and CLX. The details of the method can be found in Ref. [41].

### Inverse Kinematics

In our description of Coulomb excitation up to this point, a frame of reference has not been specified. A convenient frame of reference to use is the center of mass frame. The relation between the scattering angle in the center of mass frame  $\theta_{CM}$  and the scattering angle measured in the laboratory frame  $\theta_{lab}$  is give by

$$\frac{\sin(\theta_{CM}(n) - \theta_{lab})}{\sin \theta_{lab}} = \frac{A_1}{A_2} \left[ 1 + \frac{A_1 + A_2}{A_2} \frac{E(n)}{\epsilon_p} \right]^{-\frac{1}{2}}, \quad (3.20)$$

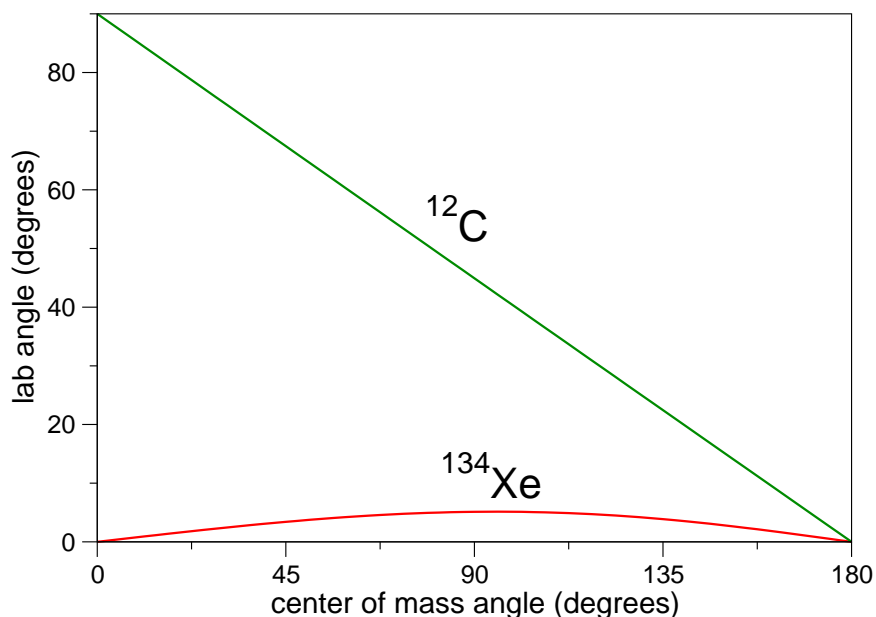


Figure 3.2: A plot showing the relation between the angles of the scattered projectile and target in the center of mass and lab frames.

where  $E(n)$  is the excitation energy of the state  $n$  and  $\epsilon_p$  is the energy of the projectile.

For scattering of light projectiles on heavy targets at moderate energies, the center of mass is approximately at the center of the target nucleus. For such a situation the measured scattering angle in the lab is approximately the same as the center of mass scattering angle as in Rutherford's scattering experiment of  $\alpha$  particles on gold nuclei. The scattering angles observed in the lab for the reverse situation of a heavy projectile scattering off of a light target can be very different from the center of mass scattering angles. This situation is called inverse kinematics. One of the consequences of inverse kinematics is the heavy projectile and the target nuclei cannot scatter at a backwards angle in the lab.

A plot showing the relationship between the lab and center of mass scattering angles of the elastic scattering of  $^{134}\text{Xe}$  nuclei and  $^{12}\text{C}$  nuclei is shown in Fig. 3.2. It can be seen that the maximum deflection of the  $^{134}\text{Xe}$  nuclei is approximately  $5^\circ$  in the lab frame. This was used to our advantage in our experiment as the energy of the Doppler shifted  $\gamma$  rays could be corrected assuming the  $^{134}\text{Xe}$  nuclei were undeflected and travelling in a definite direction, which is a good approximation for small scattering angles. Another advantage



of inverse kinematics may be the fact that the light  $^{12}\text{C}$  nuclei also scatter only in the forward direction in the lab. This may allow for higher particle detection efficiency when using only one particle detector in the forward direction.

### 3.1.2 Angular Distribution of $\gamma$ rays

For radiative decay, the intensity of the radiation as a function of direction is not isotropic in general. In this section, expressions for the angular distribution of  $\gamma$  rays that result from the decay of nuclear states excited by Coulomb excitation will be presented.

The expression for the angular distribution is given by

$$\frac{dW^{(i)}(n \rightarrow f)}{d\Omega_\gamma} = \frac{1}{\sqrt{4\pi}} \sum_{\substack{k=0,2,4 \\ -k \leq m \leq k}} A_{km}^{(i)} F_k(I_f, I_n) Y_{km}(\theta_\gamma^{(i)}, \phi_\gamma^{(i)}), \quad (3.21)$$

where  $Y_{km}(\theta_\gamma^{(i)}, \phi_\gamma^{(i)})$  are spherical harmonics and

$$F_k(I_f, I_n) = \frac{\sum_{\lambda', \lambda''} \Delta(\lambda') \Delta(\lambda'') F_k(\lambda', \lambda'', I_f, I_n)}{\sum_\lambda \Delta^2(\lambda)}, \quad (3.22)$$

where  $F_k(\lambda, \lambda', I_f, I_n)$  are the geometrical factors and are tabulated in a number of references [45–47]. The  $F_k(\lambda, \lambda', I_f, I_n)$  coefficients only depend on  $I_n$  and  $i_f$  the initial and final spins of the states, respectively, and on  $\lambda' = \lambda + 1$  and  $\lambda$ , the next to leading order and leading order multipolarity of the transition  $\gamma$  ray, respectively. The terms  $\Delta(\lambda)$  is related to the intensity of the radiation of multipolarity  $\lambda$  given by

$$\Delta(\lambda)(n \rightarrow f) = \left[ \frac{8\pi(\lambda + 1)}{\lambda[(2\lambda + 1)!!]^2} \frac{1}{\hbar} \left(\frac{\omega}{c}\right)^{2\lambda+1} \right]^{\frac{1}{2}} (2I_f + 1)^{-\frac{1}{2}} \langle I_f \| \mathcal{M}(E\lambda) \| I_n \rangle, \quad (3.23)$$

where  $\omega$  is the frequency of the radiation and  $\langle I_f \| \mathcal{M}(E\lambda) \| I_n \rangle$  is the reduced transition matrix element. This is relation to the different conventions for the multipole mixing ratio  $\delta$  can be found in Appendix A.2. The value  $A_{km}^{(i)}$  found in Eq. (3.21) is given by

$$A_{km}^{(i)} \approx \alpha_{km}^{(i)}, \quad (3.24)$$

when the level of interest is populated primarily through Coulomb excitation as opposed to decay from higher-lying states. The label  $(i)$  represents reference frame in which  $\alpha_{km}^{(i)}$  is calculated. In order to write down further expressions for  $\alpha_k^{(i)}$  a reference frame must be chosen. The reference frame for  $(i) = (0)$ ,

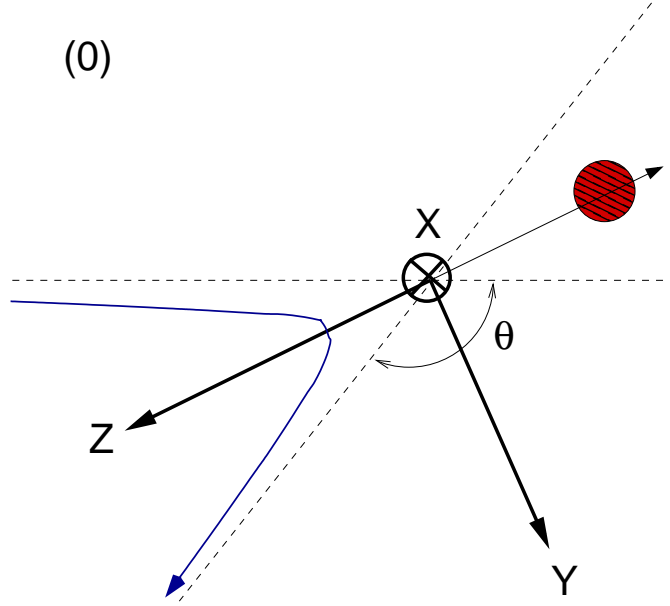


Figure 3.3: The reference frame for  $(i) = (0)$  is shown. The  $Z$  axis bisects the asymptotes of the hyperbolic path of the projectile as shown. The  $Y$  and  $Z$  axes define the plane that contains the path of the projectile.

following the numbering convention of Ref. [41], is shown in Fig. 3.3 where the  $Z$  axis bisects the asymptotes of the hyperbolic path of the projectile as shown and the  $Y$  and  $Z$  axes define the plane of the projectile's path. In this reference frame,  $\alpha_{km}^{(0)}$  is given by

$$\alpha_{km}^{(0)} = \frac{(2I_n+1)^{\frac{1}{2}}}{(2I_1+1)} \sum_{M_n=M'_n+m}^{M_n, M'_n} (-1)^{I_n+M_n} \begin{pmatrix} I_n & I_n & k \\ -M_n & M'_n & m \end{pmatrix} \quad (3.25)$$

$$\times \sum_{M_1} a_{I_n M'_n}^*(M_1) a_{I_n M_n}(M_1),$$

where  $\begin{pmatrix} I_n & I_n & k \\ -M_n & M'_n & m \end{pmatrix}$  is a Wigner 3- $j$  symbol,  $a_{I_n, M_n}(M_1)$  is the amplitude calculated for the excitation from the ground state with angular momentum and magnetic quantum numbers  $I_1$  and  $M_1$ , respectively. The values for  $\alpha_{km}^{(i)}$  for other reference frames can be found by using the expression

$$\alpha_{km}^{(i)}(n) = \sum_{-k \leq m' \leq k} D_{m'm}^k(\alpha, \beta, \gamma) \alpha_{km'}^{(0)}(n), \quad (3.26)$$

where  $D_{m'm}^k(\alpha, \beta, \gamma)$  is the rotation matrix for the Euler angles  $\alpha$ ,  $\beta$ , and  $\gamma$ .

(3)

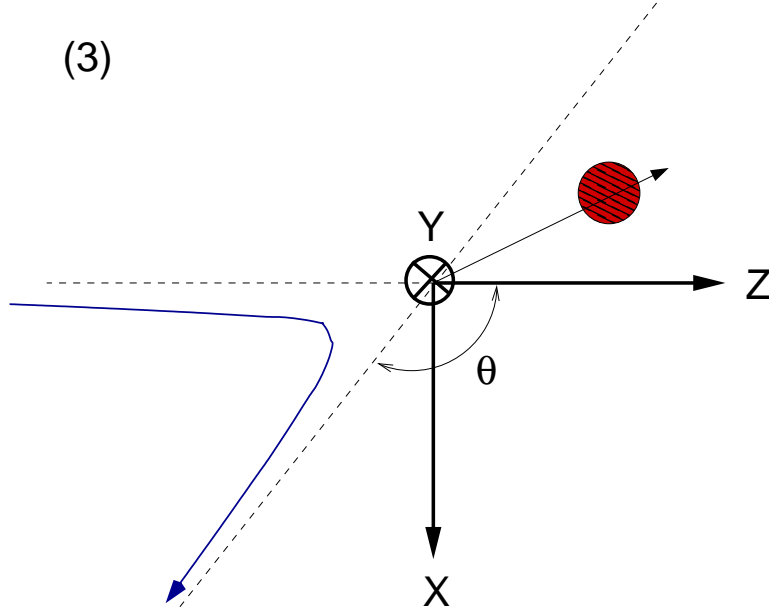


Figure 3.4: The reference frame for  $(i) = (3)$  is shown. The  $Z$  axis is parallel to the initial direction of the projectile and the  $X$  and  $Z$  axes define the plane of the projectile's path.

For the analysis of our data, the reference frame  $(i) = (3)$  will be used, continuing to follow the numbering convention of Ref. [41]. The reference frame is shown in Fig. 3.4 where the  $Z$  axis is defined to be parallel to the initial direction of the incoming projectile and the  $X$  and  $Z$  axes define the plane that contains the path of the projectile. Integrating over the azimuthal scattering angle  $\phi$ , the angular distribution of  $\gamma$  rays in this reference frame is given by

$$\frac{dW_{\text{ring}}^{(3)}(n \rightarrow f)}{d\Omega_{\gamma}} = \frac{1}{4\pi} \sum_{k=0,2,4} \alpha_{k0}^{(3)} F_k(I_f, I_n) (2k+1)^{\frac{1}{2}} P_k(\cos \theta_{\gamma}), \quad (3.27)$$

where  $P_k(\cos \theta_{\gamma})$  are the  $k$ -th order Legendre polynomials. This will be the primary expression that will be used in the analysis of measured angular distributions.

# Chapter 4

## Experiment and Data Analysis

### 4.1 Experiment

The Coulomb excitation experiment was performed at the ATLAS facility in Argonne National Laboratory located in Argonne, IL. The facility hosts a superconducting linear accelerator ATLAS, which uses niobium resonators cooled down to liquid helium temperatures. It is able to accelerate a large array of isotopes to energies of 7-17 MeV/u. The two types of ion sources are available for the accelerator, an ECR source which feeds a linac injector and a sputter source which is injected with a Tandem Van de Graaff accelerator.

The Coulomb excitation experiment with  $^{134}\text{Xe}$  and  $^{136}\text{Ce}$  beams was ATLAS experiment 1085 and Gammasphere experiment GSFMA170. The first isotope to be measured was  $^{134}\text{Xe}$ . A beam of  $^{134}\text{Xe}$  was accelerated to an energy of 435 MeV, which corresponds to 86% of the Coulomb barrier, onto a 1.0 mg/cm<sup>2</sup> natural carbon target. The intensity of the beam was approximately 1 pA and the duration of the measurement was 38 hours. Similarly a beam of  $^{136}\text{Ce}$  was accelerated to an energy of 475 MeV, also corresponding to 86% of the Coulomb barrier, with a beam intensity of 1 pA onto the same natural carbon target. The duration of the  $^{136}\text{Ce}$  measurement was similar to that of  $^{134}\text{Xe}$ .

The reason for choosing carbon as a target is two-fold. First, the first excited state of  $^{12}\text{C}$ , which has a 98.9% natural abundance, is at 4.4 MeV and therefore the probability of exciting this state with respect to the nuclei of interest is small. Even if it was excited, the emitted  $\gamma$  ray is at a high enough energy that it should not interfere with the energy region of interest, namely 500 keV to 2.5 MeV. The much less abundant  $^{13}\text{C}$  also has a first excited state at a high excitation energy of 3.1 MeV. Due to this and its low abundance of 1.1%, it was assumed that there was not much of a contribution of  $^{13}\text{C}$  in

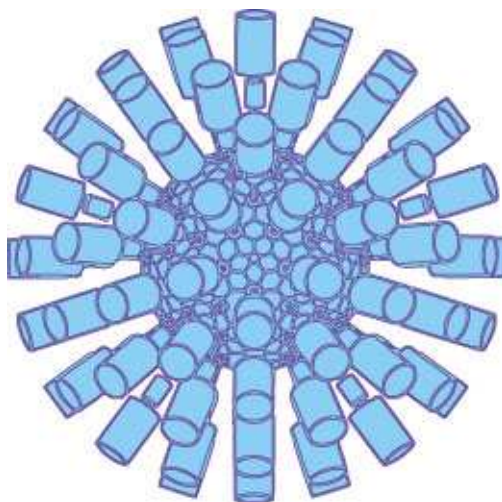


Figure 4.1: The a drawing of the Gammasphere array is shown. It consists of 110 HPGe detectors arranged spherically. The faces of the detectors form a 122-element polyhedron consisting of 110 hexagons and 12 pentagons. (Figure from Ref. [50])

the spectra. Second, carbon was used due to its relatively low atomic number  $Z = 6$  to prevent a large cross section for multistep Coulomb excitation since the focus of the experiment was to study low-spin collective states.

### Gammasphere

The Gammasphere array is an array of 110 high-purity Ge (HPGe) detectors with Compton suppression shields. Details for the array can be found in Refs. [48, 49]. A drawing showing the geometry of Gammasphere is shown in Fig. 4.1. It can be seen that the detectors are arranged symmetrically in roughly a sphere with the faces of the detector forming a 122-element polyhedron. The polyhedron consists of 110 hexagons, which are occupied by the detectors and 12 pentagons, which are openings in the polyhedron for target chamber mounts and auxiliary detectors. A schematic diagram for the Gammasphere detectors is shown in Fig. 4.2. All of the detectors cover 46% of the total solid angle. Each of the detectors have an efficiency of 82% at 1.33 MeV with respect to the NaI standard and the entire array has a total photopeak efficiency of 9.4%. The  $\gamma$  rays from the target are collimated with Hevimet, a dense metal alloy, which also shields the BGO elements of the BGO shield. The  $\gamma$  rays that are Compton scattered into the BGO shields are detected and the signal is used as a veto to suppress Ge signals that do not contain the full



Figure 4.2: A schematic diagram of Gammasphere HPGe detectors. It consists of a HPGe crystal, BGO anti-Compton elements, photomultipliers for the BGO elements, Hevimet collimators, detector electronics, and a liquid nitrogen dewar, which stores liquid nitrogen for cooling the HPGe crystal. (Figure from Ref. [50])

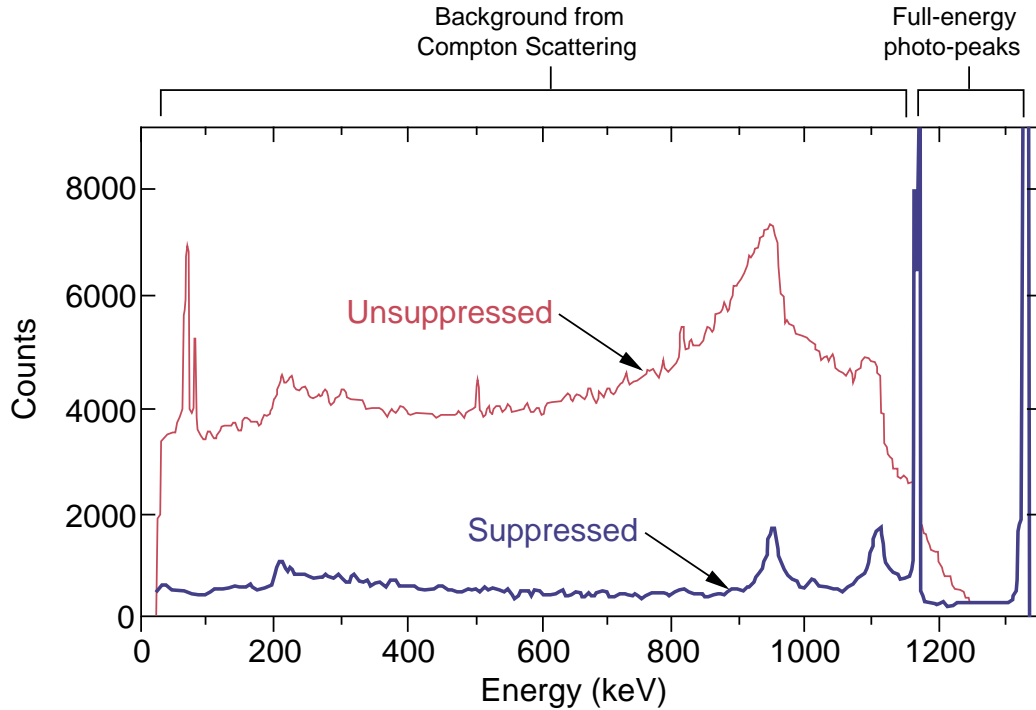


Figure 4.3: Two energy spectra are shown for data obtained from a  $^{60}\text{Co}$  source with and without Compton suppression. (Figure from Ref. [50])

$\gamma$ -ray energy. A unique element of the Gammasphere detectors is the BGO backplug, which can be seen in the figure. This BGO element used for Compton suppression is especially useful in that the Compton scattering cross section is large at angles close to  $0^\circ$  and  $180^\circ$ . Two spectra illustrating the effect of Compton suppression is shown in Fig. 4.3 for data obtained from a  $^{60}\text{Co}$  source. The Compton unsuppressed spectrum shows the large Compton background that comes from  $\gamma$  rays that deposit only a portion of their full energy in the Ge crystal. The Compton suppressed spectrum shows a much lower Compton background that results from vetoing Compton scattered  $\gamma$  rays detected in one of the BGO elements.

### Spectra and Level Schemes

An energy spectrum for  $^{134}\text{Xe}$  obtained from the sum of all detectors is shown in Fig. 4.4.

The spectrum was corrected for the Doppler shift due to the moving ion and background subtracted. These methods will be discussed in more detail

$^{12}\text{C}(^{134}\text{Xe}, ^{134}\text{Xe}^*)^{12}\text{C}$   
Singles spectrum

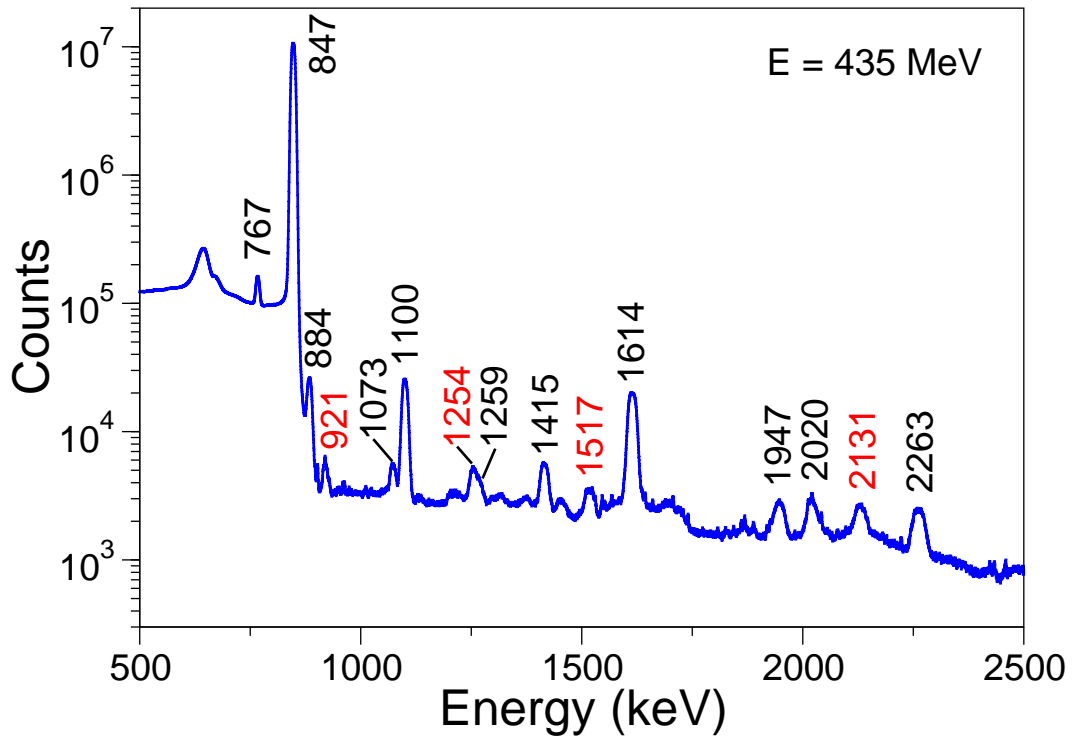


Figure 4.4: An energy spectrum for  $^{134}\text{Xe}$  for the sum of all Gammasphere detectors.



$^{12}\text{C}(^{136}\text{Ce}, ^{136}\text{Ce}^*)^{12}\text{C}$   
Singles spectrum

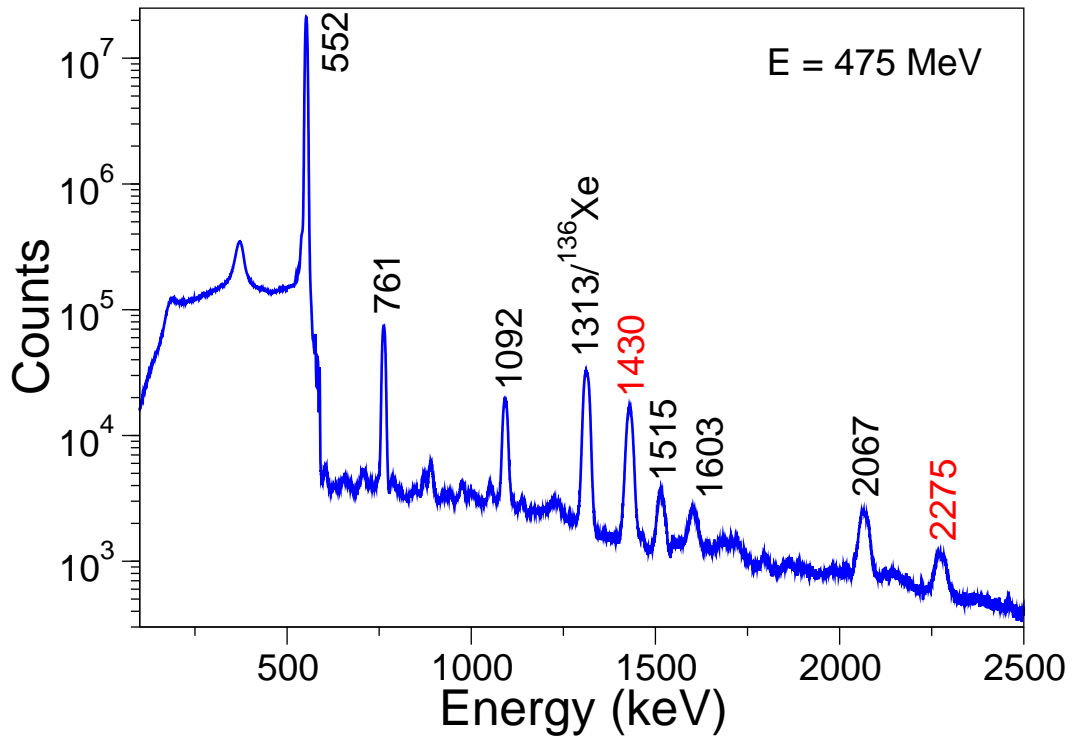


Figure 4.5: An energy spectrum for  $^{136}\text{Ce}$  for the sum of all Gammasphere detectors.

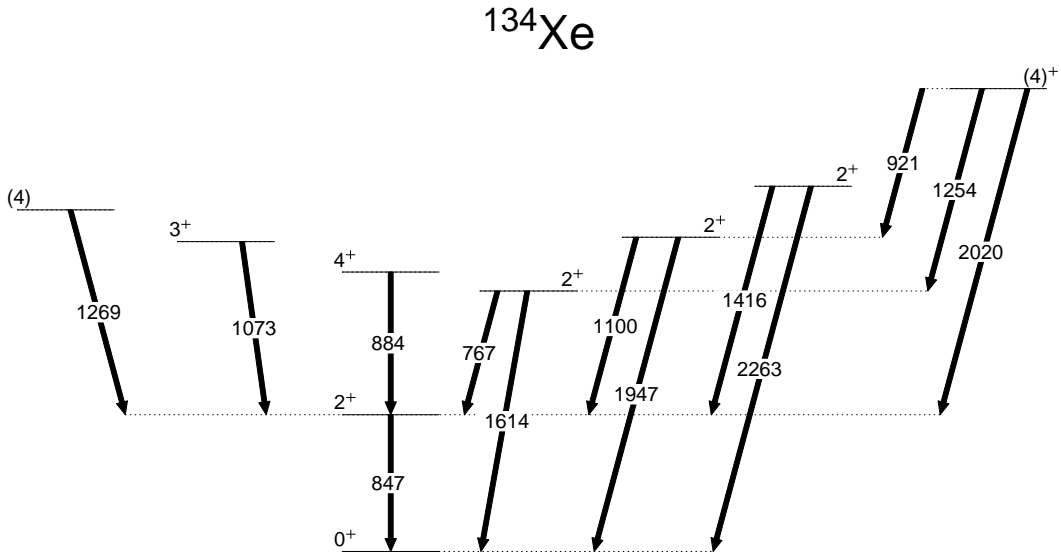


Figure 4.6: Level scheme for the observed transitions and corresponding levels in  $^{134}\text{Xe}$ .

in the following sections. A level scheme for  $^{134}\text{Xe}$  and  $^{136}\text{Ce}$  showing the observed transitions and their corresponding levels is shown in Figs. 4.6 and 4.7, respectively.

## 4.2 Data Analysis

The experimental data were stored in a format called list mode, where data for each event were recorded and individually stored on magnetic tape or hard disk. All data were sorted offline to produce the final spectra and matrices. The events in our experiment were defined as the detection of one or more  $\gamma$  rays not Compton suppressed in any of the detectors. A total of  $8.4 \times 10^8$  events were recorded for  $^{134}\text{Xe}$  experiment and  $7.8 \times 10^8$  events for the  $^{136}\text{Ce}$  experiment. The Multi Instance Data Acquisition System (MIDAS) program using the MTSort language was used to sort the raw data into spectra and matrices.

### 4.2.1 Efficiency Calibration

An efficiency calibration was done using  $^{152}\text{Eu}$  and  $^{56}\text{Co}$  sources mounted at the position of the beam spot. The use of both sources provided  $\gamma$  rays

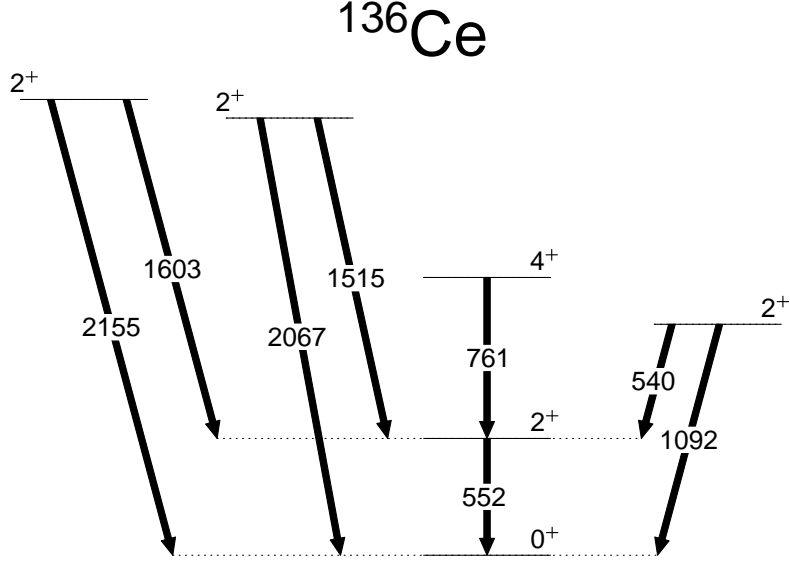


Figure 4.7: Level scheme for the observed transitions and corresponding levels in  $^{136}\text{Ce}$ .

with energies covering the energy range of interest, from 300 keV to 2.6 MeV. A figure showing the relative efficiency measured for the set of Gammasphere detectors at an angle  $\theta = 90^\circ$ . is shown in Fig. 4.8. A precise efficiency calibration was crucial in measuring the relative cross sections of states excited in Coulomb excitation and angular distributions. The magnitude of how precisely the relative efficiency could be measured was limited by the statistics accumulated for each  $\gamma$  ray peak and the precision to which the relative efficiencies of the  $\gamma$  rays were known. Both of these uncertainties were on the order of 1%. This means that all measured intensities were limited in precision by roughly this amount.

## 4.2.2 Doppler Correction

For each experiment, a  $1.2 \text{ mg/cm}^2$  natural carbon target was used. The thickness of the target was not sufficient to stop any ions traversing through it and all ions recoiled into vacuum. The velocity of the ions was on the order of 6-7% the speed of light. This resulted in a Doppler shift of observed  $\gamma$  rays. The relativistic Doppler formula is given by

$$E(\theta) = E_0 \frac{(1 + \beta \cos \theta)}{\sqrt{1 - \beta^2}}, \quad (4.1)$$

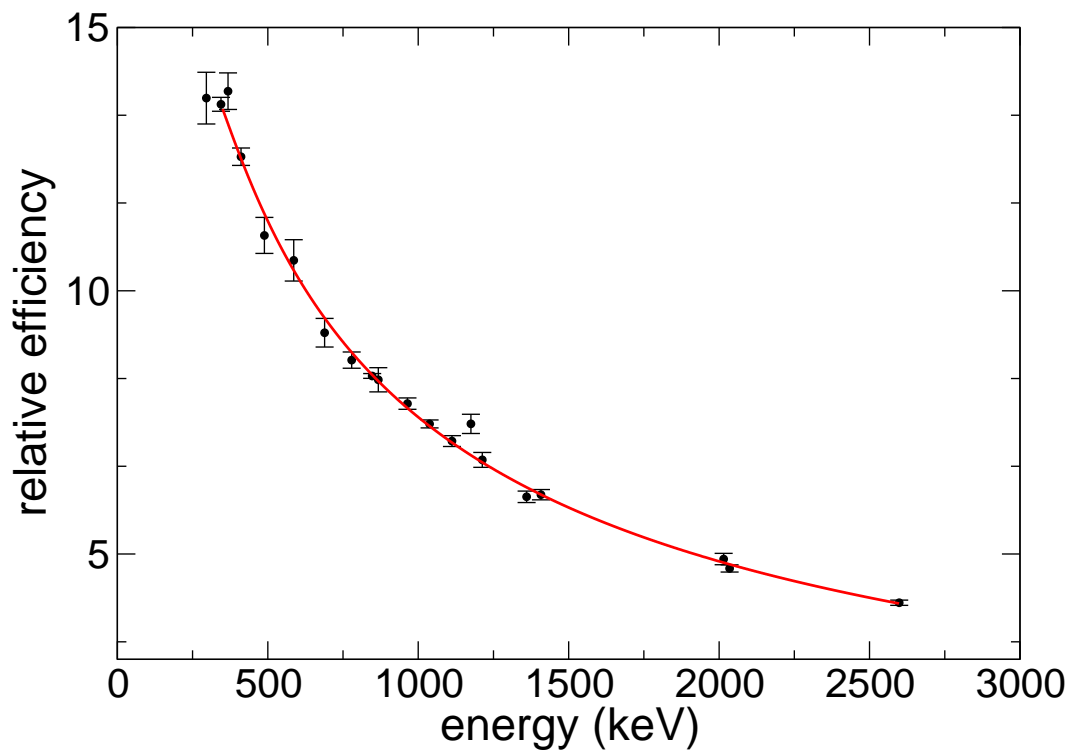


Figure 4.8: The measured relative efficiency and the fitted efficiency curve for the set of Gammasphere detectors at  $90^\circ$ .

where  $E_0$  is the Doppler unshifted energy,  $\theta$  is the angle of the detector with respect to the beam axis, and  $\beta = \frac{v}{c}$ . Assuming that the heavy ions travel in a straight line down the beam axis, which is reasonable approximation for a heavy projectile and light target, the observed  $\gamma$ -ray energy was corrected to the Doppler unshifted energy  $E_0$ .

### Using Gammasphere's Segmented Detectors

The increase in the width of a doppler shifted peak due to the finite angular size of a  $\gamma$ -ray detector is called Doppler broadening. The magnitude of this broadening is obtained by differentiating Eq. (4.1) with respect to  $\theta$  obtaining

$$dE = E_0 \frac{\beta \sin \theta}{\sqrt{1 - \beta^2}} d\theta. \quad (4.2)$$

It can be seen that this effect is maximum for detectors located at  $90^\circ$  with respect to the velocity of the recoiling nucleus emitting the  $\gamma$  ray. A number of Gammasphere detectors have a two-fold segmentation of the outer electrode and information from this segmentation can be used to increase the angular granularity of the array by allowing one to know which part of the detector the  $\gamma$  ray was detected. A figure illustrating the use of segmentation is shown in Fig. 4.9. Most of the segmented detectors are located at and around  $90^\circ$  where the broadening is largest.

A  $\gamma$  ray interacting at different points in the detector will exhibit different Doppler shifts. This can be seen in Fig. 4.10, where three different peaks are shown corresponding to a  $\gamma$  ray being detected in the three different regions of the detector called left, center, and right. In the present work, a three-fold partition of the detector was used. It can be seen that the energy of each peak is Doppler shifted according to whether the location of the portion of the detector corresponding to left and right were at a smaller or larger angle with respect to the beam axis. In this case, left corresponded to a larger angle  $\theta$  while right corresponded to a smaller angle  $\theta$ .

A Gammasphere detector covers an angle of  $7.4^\circ$ . For a 1 MeV  $\gamma$  ray and  $\beta = 0.07$ , the Doppler broadening is 9.0 keV. If the uncertainty in the angle is reduced by a factor of two, the Doppler broadening is reduced to 4.5 keV. It can be seen in Fig. 4.10 that the resolution of a peak is still larger than what can be accounted for from Doppler broadening alone. The uncertainty in the velocity of the beam  $\Delta\beta$  and the intrinsic detector resolution  $\Delta E_{\text{det}}$  also contribute to the width of a peak. The relative width of a peak is given by

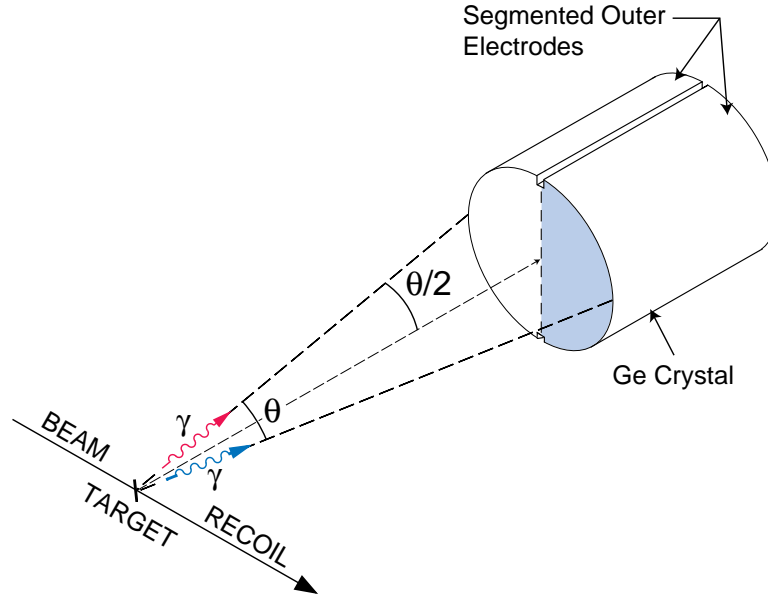


Figure 4.9: Shown is the segmentation of the outer electrode of segmented Gammasphere detectors. A  $\gamma$  ray hitting different parts of the detector will have different Doppler shifts. (Figure from Ref. [50])

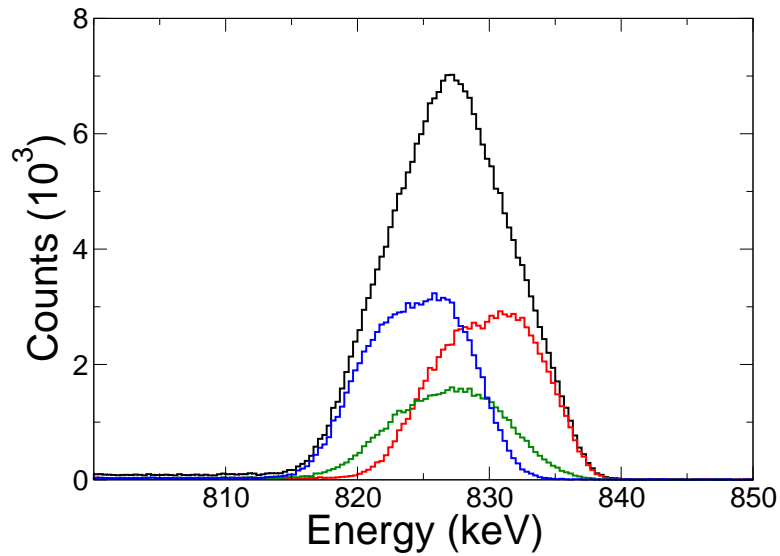


Figure 4.10: Spectrum of peaks from one of the Gammasphere detectors separated into left hit, center hit, and right hit is plotted in red, green, and blue, respectively.

summing the contributions in quadrature as

$$\left(\frac{\Delta E}{E}\right)^2 = \left(\frac{\beta \sin \theta}{1 - \beta \cos \theta}\right)^2 (\Delta \theta)^2 + \left(\frac{-\beta + \cos \theta}{(1 - \beta^2)(1 - \beta \cos \theta)}\right)^2 (\Delta \beta)^2 + \left(\frac{\Delta E_{\text{det}}}{E}\right)^2, \quad (4.3)$$

where  $\Delta E$  is the total width of a peak,  $E$  is the energy of the  $\gamma$  ray, and  $\Delta \theta$  is the uncertainty in the  $\gamma$  ray detection angle due to the finite solid angle of a detector and the spread in angle due to the scattering of the projectile [51]. With these additional terms, the total width of the peak should be accounted for.

### 4.2.3 Room Background Subtraction

In the experiment, the  $\gamma$  rays coming from the natural room background were contaminants in the energy spectra. Because peak areas need to be measured as accurately as possible for the measurement of cross sections and angular distributions, any method to filter out or subtract these contaminants is desirable. A portion of the time-energy matrix for the  $^{134}\text{Xe}$  measurement is shown in Fig. 4.11. Time runs from right to left on the x-axis of the plot. The features corresponding to peaks originating from Coulomb excitation and room background can be seen. Whereas the Coulomb excitation lines happen at roughly one point in time, corresponding to when the beam bunch of ions hits the target, the room background lines are uniform in time. Because the room background is constant, one can subtract the contribution of the room background by setting gates on different parts of the time spectrum. A typical time spectrum and the relevant gates are shown in Fig. 4.12. The spectrum resulting from the background gates can be subtracted from the spectrum resulting from the beam gate in order to subtract the background. In order to do this, the spectrum obtained from the background gate has to be properly normalized. This can be done by taking the ratios of the width of the beam gate  $W_{\text{beam}}$  and background gates  $W_{\text{back}} = \sum_i W_{\text{back}}^i$ . The background subtracted spectrum is then obtained by

$$N_{\text{sub}}(E_i) = N_{\text{beam}}(E_i) - \frac{W_{\text{beam}}}{W_{\text{back}}} N_{\text{back}}(E_i). \quad (4.4)$$

The results of the background subtraction for a Doppler uncorrected spectrum is shown in Fig. 4.13. Part (a) of the figure shows the 1461-keV line from the decay of the naturally occurring  $^{40}\text{K}$ . It can be seen in Part (b) the line is

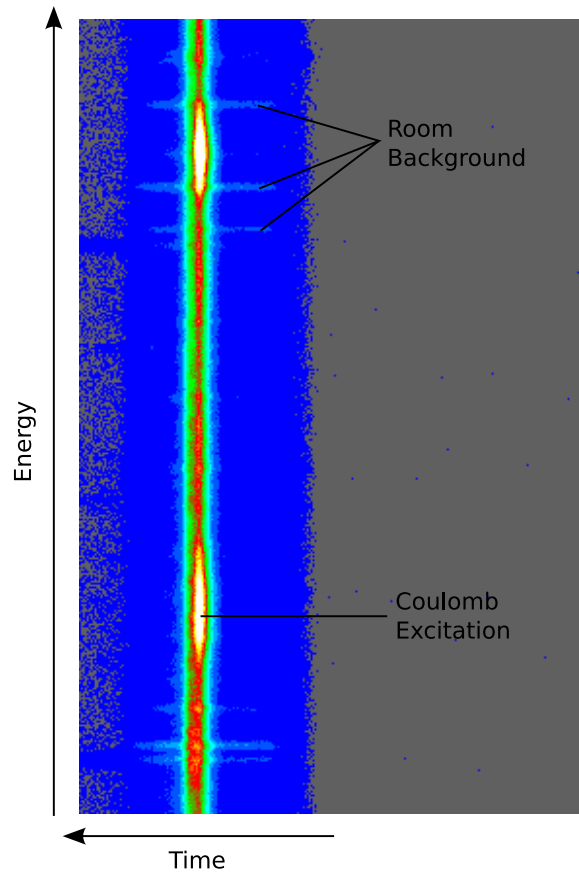


Figure 4.11: Part of the time-energy matrix is shown. The peaks corresponding to room background and Coulomb excitation can be seen.



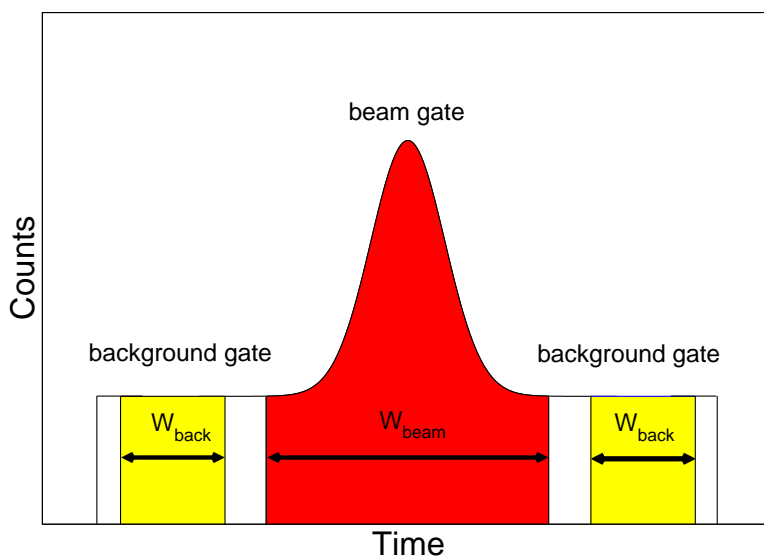


Figure 4.12: Illustration of time spectrum and the beam and background gates set on it.

completely subtracted. In Part (c) of the spectrum, two background lines can be seen. The higher energy line comes from the decay of Th. Part (d) shows the Th line is subtracted while the other background line is hardly reduced. This means that the latter background line is correlated in time with the beam and cannot be subtracted using time gates. This is one possible source of systematic error in the measured peak areas.

#### 4.2.4 Measuring Angular Distributions of $\gamma$ Rays

Angular distributions of  $\gamma$  rays were measured using Gammasphere. The detectors were grouped into sets of detectors that were at the same polar angle  $\theta$  from the beam axis. There were a total of 16 different sets, also known as rings, for our experiment, which allowed for measurements of intensities at maximally 16 different angles.

#### Relativistic Effects

The beam velocities of the ions in the experiment were on the order of 7% the speed of light. These velocities were sufficient to produce observable relativistic effects that change the angle of propagation of a  $\gamma$  ray. This results in a change in the angle and solid angle of a detector when viewed from the projectile nucleus' frame of reference. These effects had to be accounted for

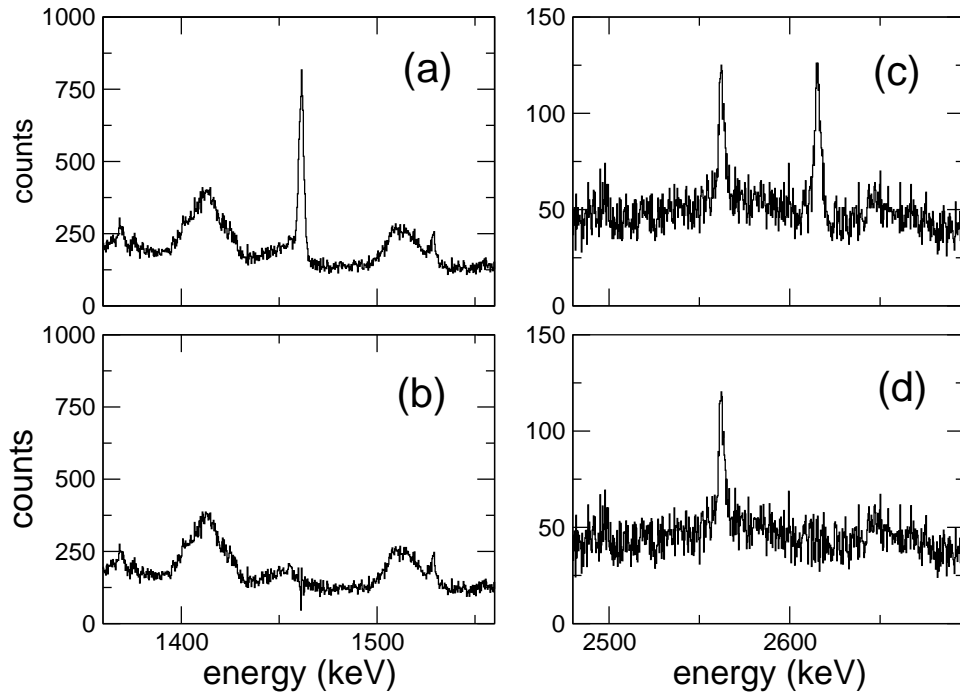


Figure 4.13: A parts of a Doppler-uncorrected energy spectrum are shown with and without subtraction using time gates. Part (a) shows the 1461-keV peak from the decay of naturally occurring  $^{40}\text{K}$ . Part (b) shows it subtracted. Part (c) shows two background lines, one of which is the peak coming from the decay of Th. Part (d) shows the Th line subtracted while the other remains.

in order to measure proper angular distributions. The expression relating the angle of a detector in the lab  $\theta_{\text{lab}}$  and the angle of a detector in the nuclear frame of reference  $\theta_{\text{nuc}}$  is given by

$$\cos \theta_{\text{nuc}} = \frac{\cos \theta_{\text{lab}}}{1 - \beta \cos \theta_{\text{lab}}}, \quad (4.5)$$

where  $\beta = \frac{v}{c}$  [52]. The maximum change in the angle occurs at  $\theta_{\text{lab}} = \frac{\pi}{2}$  and with the change becoming smaller as one goes to either  $0^\circ$  or  $180^\circ$ , where there is no change in angle between the lab and nuclear reference frames. This can easily be derived by differentiating the expression for  $\theta_{\text{lab}}$  and seeing that the expression is proportional to  $\sin \theta_{\text{lab}}$ .

For velocities of  $\beta = 0.07$  as in our experiment, the largest change in angle is about 3 degrees. This does not dramatically influence our angular distributions, but is an observable effect that can be accounted for. One of the effects is that there is a finite Doppler shift for detectors that are located at  $90^\circ$  in the laboratory frame.

Another effect, which is much more significant for our analysis is the change in the apparent solid angle of detectors, which results from the change in propagation angle of the emitted photon. This result can be derived from the Eq. 4.5. The relation for the solid and in the lab frame  $d\Omega_{\text{lab}}$  and in the nuclear frame  $d\Omega_{\text{nuc}}$  is given by

$$d\Omega_{\text{nuc}} = \frac{1 + \beta \cos \theta_{\text{nuc}}}{1 - \beta^2} d\Omega_{\text{lab}}. \quad (4.6)$$

The maximum for the change in solid angle occurs at  $0^\circ$  and  $180^\circ$  and for velocities  $\beta = 0.07$  the change in solid angle at  $0^\circ$  is 13%.

## Measuring Multipole Mixing Ratios

The measurement of the angular distribution of  $\gamma$  rays allows one to measure the multipole mixing ratios for mixed transitions, which is needed to deduce  $M1$  transition strengths. The decay of a  $2^+$  state in a vibrational nucleus is shown in Fig. 4.14. The  $2^+$  state can decay either through a pure  $E2$  transition to the ground state or a mixed  $E2/M1$  transition to a lower-lying  $2^+$  state. For the one-quadrupole phonon  $2^+_{1,\text{ms}}$  mixed-symmetry state, we are interested in measuring the  $E2/M1$  multipole mixing ratio of decays to the  $2^+_1$  state.

An excited  $2^+$  state is primarily populated by Coulomb excitation. The excitation process aligns the state meaning there is a non-uniform population of various  $M$  states. The alignment of the states is quantified by the so called

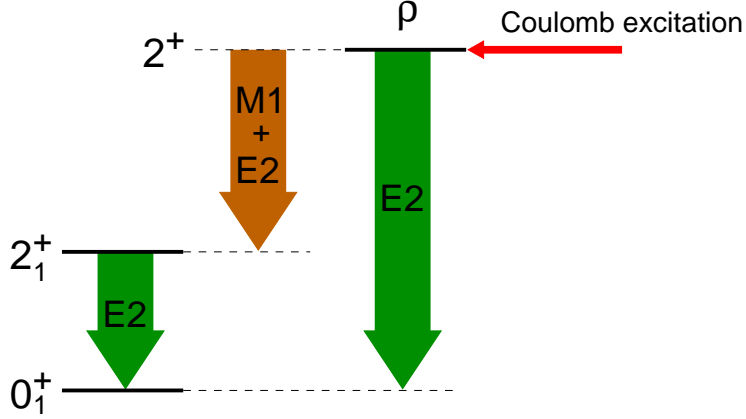


Figure 4.14: The decay of a  $2^+$  excited state.

statistical tensors  $\rho_k(I)$  [53], which are related to the relative population of  $M$  states  $P_M(I)$  by

$$\rho_k(I) = (2I + 1)^{\frac{1}{2}} \sum_M (-1)^{I-M} \langle I M I - M | k 0 \rangle P_M(I), \quad (4.7)$$

where  $\langle I M I - M | k 0 \rangle$  is a Clebsch-Gordon coefficient. This non-uniform population of the  $M$  states is what gives rise to the observed anisotropic distribution of radiation. The statistical tensors are equal to the terms  $\alpha_{km}^{(i)}$  defined in Eqs. 3.25 and 3.26 apart from a constant.

First the angular distribution of the decay to the ground state is measured to obtain the values for the statistical tensors. The measured angular distribution for the  $2_2^+ \rightarrow 2_1^+$  decay in  $^{134}\text{Xe}$  is shown in Fig. 4.15. The data were fitted with the function

$$W(\theta) = \sum_{k=0,2,4} C_k P_k(\cos \theta), \quad (4.8)$$

which is a parameterized version of Eq. (3.27) where  $C_k$  are parameters and  $P_k(\cos \theta)$  are the  $k$ -th order Legendre polynomials. The function was fitted using a  $\chi^2$  minimization procedure. The parameters  $C_k$  are related to the statistical tensors by

$$A_k = \rho_k(I) C_k'(\lambda, \lambda', I_f, I_n, \delta), \quad (4.9)$$

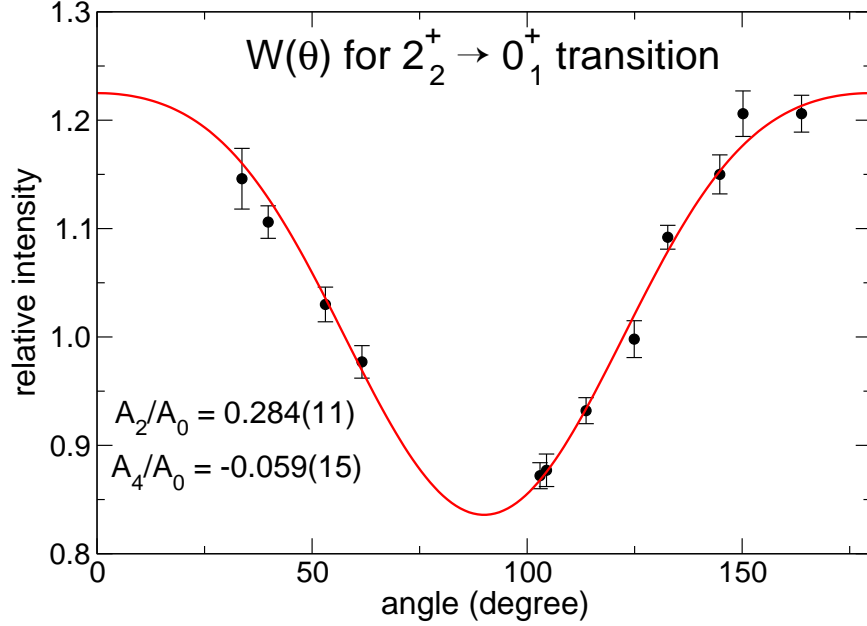


Figure 4.15: The measured and fitted angular distribution function  $W(\theta)$  for the 1614-keV transition in  $^{134}\text{Xe}$ .

where

$$C'_k(\lambda, \lambda', I_f, I_n, \delta) = \frac{F_k(\lambda, \lambda, I_f, I_n) + \delta F_k(\lambda, \lambda', I_f, I_n) + \delta^2 F_k(\lambda', \lambda', I_f, I_n)}{1 + \delta^2}. \quad (4.10)$$

The terms  $F_k(\lambda, \lambda', I_f, I_n)$  are the  $F$  coefficients mentioned in Sec. 3.1.2 and the multipole mixing ratio  $\delta$  is defined as

$$\delta = q \frac{\sqrt{3} \langle I_f \| \mathcal{M}(E2) \| I_n \rangle}{10 \langle I_f \| \mathcal{M}(M1) \| I_n \rangle}, \quad (4.11)$$

where the reduced transition matrix elements contain the multipole operators defined in Eq. 3.11 and

$$\mathcal{M}(M\lambda, \mu) = \frac{-1}{c(\lambda + 1)} \int \mathbf{j}(\mathbf{r}) \cdot (\mathbf{r} \times \nabla) r^\lambda Y_{\lambda\mu}(\theta, \phi) d^3r. \quad (4.12)$$

The term  $C'_k$  is equivalent to the term  $F(I_f, I_n)$  defined in Eq. 3.22, the only difference being written in terms of  $\delta$  or  $\Delta(\lambda)$ . The relation of  $\delta$  and  $\Delta(\lambda)$  with the multipole operators as well as the various conventions used for  $\delta$  can be found in Appendix A.

$J_i^\pi$	$\rho_2$	$\rho_4$
$2_1^+$	-0.20(7)	0.0(24)
$2_2^+$	-0.48(5)	0.1(4)
$2_3^+$	-0.512*	0.069*
$2_4^+$	-0.538*	0.085*

Table 4.1: Table of  $\rho_n$  coefficients for  $2^+$  states in  $^{134}\text{Xe}$ . The values marked with an \* were calculated from first-order perturbation theory for a beam energy of 435 MeV.

The values of  $\rho_k(I)$  from the fitted values of  $C_k$  can be found using Eqs. (4.9) and (4.10). The calculated values of the statistical tensors of the  $2^+$  states of  $^{134}\text{Xe}$  are tabulated in Table 4.1. The statistical tensors for the  $2_3^+$  and  $2_4^+$  states were not calculated from the measurement of the angular distribution coefficients as were the values for the  $2_1^+$  and  $2_2^+$  states. The reason is because the relevant peaks had background contamination, which could not be subtracted from the spectrum. The statistical tensors for these states were calculated from Coulomb excitation amplitudes calculated from first-order perturbation theory. It was assumed that second and higher order effects such as multiple step Coulomb excitation to these states would be small due to the relatively high excitation energy of the states and also a lack of strong  $E2$  transitions connecting it with the  $2_1^+$  state. The relative population of  $M$  states calculated from the statistical tensors listed in Table 4.1 is shown in Fig. 4.16. It can be seen that the alignment of higher-lying states is higher than the  $2_1^+$  state. This may be due to a deorientation from hyperfine fields as the ions leave the target and recoil into vacuum. The relatively short lifetimes of the higher-lying states may have prevented a large attenuation from this effect.

After the statistical tensors for the states of interest are known,  $\delta$  of the mixed transition to the  $2_1^+$  state can be found by performing a fit of the angular distribution using  $\delta$  as a parameter. Using Eqs. (4.9) and (4.10), the angular distribution function given in Eq. (4.8) can be parameterized by  $\delta$  and  $C_0$ . The angular distribution for the  $2_2^+ \rightarrow 2_1^+$  is shown in Fig. 4.17. The results for  $\delta$  for the mixed transitions in  $^{134}\text{Xe}$  are tabulated in Table 4.2. For the  $2^+ \rightarrow 0_1^+$  transitions in  $^{136}\text{Ce}$ , the low intensity of these transitions along with background contamination resulted in not being able to make any clean measurements of  $\delta$ . For later analysis, the multipole mixing ratios were taken from Ref. [54] where they were measured in an  $\gamma\gamma$  angular correlation measurement.

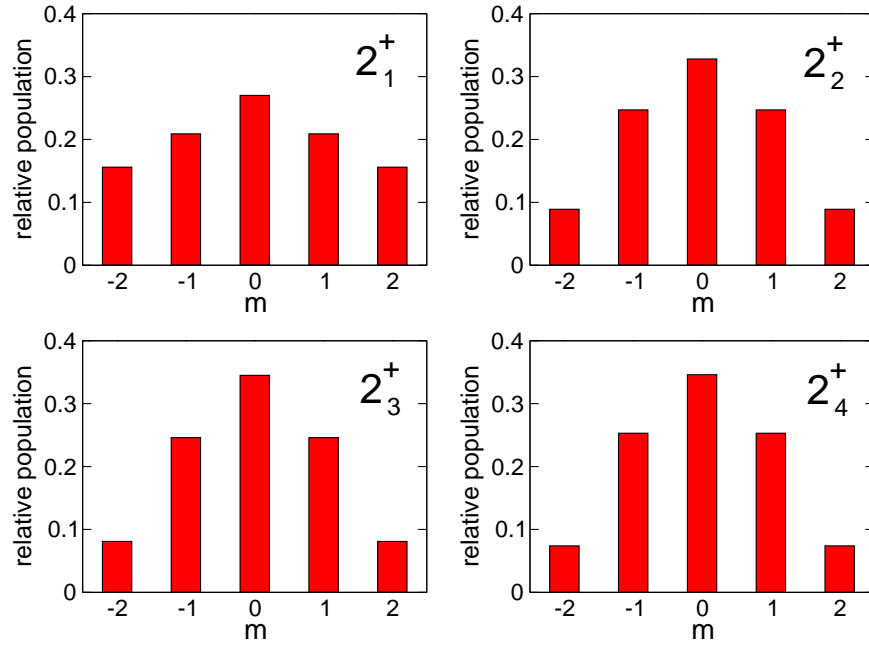


Figure 4.16: The relative population of  $M$  states of  $2^+$  states of  $^{134}\text{Xe}$  is shown.

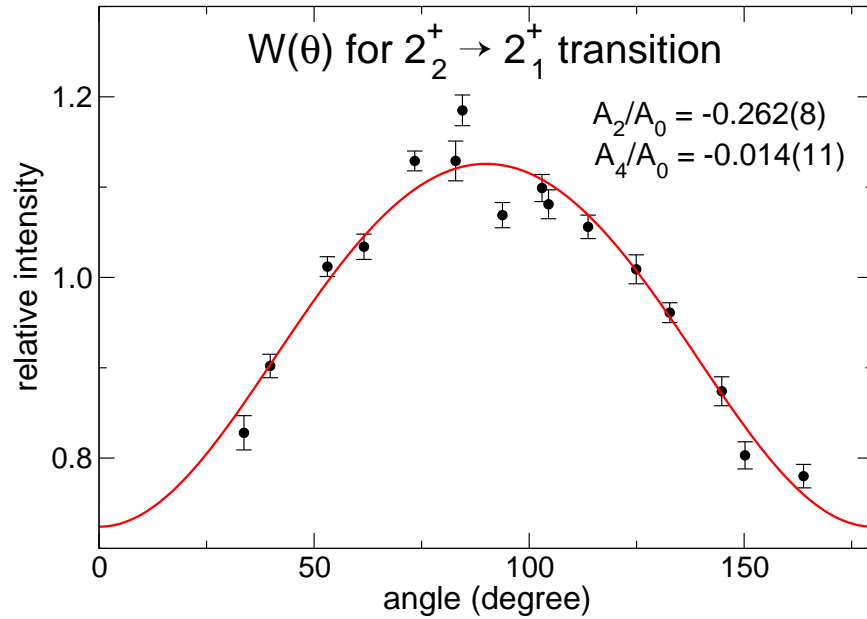


Figure 4.17: The measured and fitted angular distribution function  $W(\theta)$  for the 767-keV transition in  $^{134}\text{Xe}$ .

### 4.2.5 Transition Matrix Elements from Coulomb Excitation Cross Sections

From the observed transition intensities, one is able to calculate the relative population for each of the observed states and thus the relative Coulomb excitation cross section. This is done by adding and subtracting the  $\gamma$ -ray intensities according to the known level schemes, given in Figs. 4.6, 4.7, to account for the population of a state from a  $\gamma$  transition from a higher-lying state. The observed intensity of each transition is tabulated in Tables 4.2 and 4.3 for  $^{134}\text{Xe}$  and  $^{136}\text{Ce}$ , respectively. The intensities were normalized to the respective  $2_1^+ \rightarrow 0_1^+$  transitions.

Two different Coulomb excitation programs, CLX and GOSIA, were used to determine the transition matrix elements. Each of the programs and how they were used will be described, especially the CLX program due to its extensive use in the analysis.

#### CLX

One of the programs used was CLX [43, 44], which is a modified version of the multiple Coulomb excitation program developed by Winther and de Boer [41]. The main difference between the CLX program and the Winther and de Boer program is the Winther de Boer program can calculate cross sections for  $E2$  excitations for up to 10 nuclear levels. The modified CLX can calculate cross sections for up to 50 states and for  $E1$ ,  $E2$ ,  $E3$ ,  $E4$ , and  $M1$  transitions. Otherwise, CLX uses the same algorithms for calculating the Coulomb excitation amplitudes as in the program of Winther and de Boer. This procedure will briefly be outlined below.

The program of Winther and de Boer calculates the Coulomb excitation amplitudes by integrating the set of coupled differential equations as given by Eq. 3.9, which is explained in detail in Ref. [41].

Starting with the coupled differential equations for the Coulomb excitation amplitudes given in Eq. 3.9, the equations can be transformed by the change of variables

$$t = \frac{a}{v}(\epsilon \sinh w + w), \quad (4.13)$$

$$r_p(t) = a(\epsilon \cosh w + 1), \quad (4.14)$$



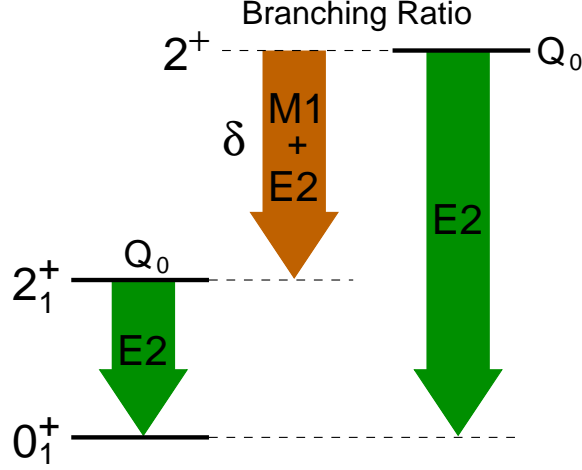


Figure 4.18: A  $2^+$  state decaying to the  $2_1^+$  state and  $0_1^+$  ground state. The matrix elements for the transitions, the quadrupole moments of the states  $Q_0$  are input parameters of the program. The branching ratio and multipole mixing ratio  $\delta$  put constraints on the value of the matrix elements.

where  $\epsilon = \frac{1}{\sin \frac{\theta}{2}}$ . The differential equations then become

$$\frac{da_n(w)}{dw} = \frac{4\pi Z_1 e}{i\hbar v} \sum_{\lambda\mu m} \frac{Y_{\lambda\mu}(\theta, \phi) \exp[i\xi_{nm}(\epsilon \sinh w + w)]}{a^\lambda (\epsilon \cosh w + 1)^\lambda (2\lambda + 1)} \langle m | \mathcal{M}(E\lambda, \mu) | n \rangle a_m(w). \quad (4.15)$$

Further simplifications can be made by defining several new variables and using symmetry relations, but the integration performed by the program is basically Eq. (4.15) over the variable  $w$ . For the integration of Eq. (4.15), a fourth-order Runge-Kutta method is used to find the initial values that are input into an Adams-Moulton predictor-corrector method. An adaptive stepsize is used to ensure that the accuracy defined by the user is maintained.

Shown in Fig. 4.18 is again the decay of a  $2^+$  state to the  $2_1^+$  and  $0_1^+$  ground state. The transition matrix elements corresponding to the shown transitions are input parameters in the program. The electric quadrupole moments are the diagonal matrix elements of the  $E2$  operator and they are also input parameters in the program. The modification of cross sections due to the quadrupole moment of a state is a second-order effect. Due to this and the fact that the quadrupole moment for vibrational nuclei are not large, a value of  $Q_0 = 0$  for all states were assumed. The  $E2$  transitions are the dominant mode of excitation in vibrational nuclei and thus the  $M1$  transition

matrix element does not contribute much to the total cross section. It is for this reason the multipole mixing ratio  $\delta$  is important for constraining the  $M1$  matrix element. The branching ratios, which are either known or easily measured for almost all states of interest place another important constraint on the matrix elements.

A set of matrix elements was to input a set of matrix elements in the program and the corresponding cross sections were calculated. Then these cross sections were compared with the experimental ones and then changed accordingly to reproduce the experimental cross sections using the measured or known branching ratios and multipole mixing ratios were used to constrain the ratio of matrix elements. The starting values for the matrix elements were calculated from the ratio of cross sections calculated from first-order perturbation theory as found in Ref. [38]. The values of these matrix elements were found to be close to the ones calculated from the CLX program, although slightly they were slightly overestimated.

One of the unknown parameters in the calculation was determining the relative phase of the matrix elements. The RPT phase convention [39] is used in the program, which gives real values for the matrix elements, but the value can either be positive or negative. Use of different phases corresponding to the positive or negative value of the matrix elements can modify the cross sections due to interference effects. Strictly speaking, in this way the values of the matrix elements are not uniquely determined by the experimentally observed cross sections. Despite this, the interference effects are second-order effects and the extent to which they affect the values of the matrix elements in our experiment is small.

### **Integrating over Energy Loss in Target**

Charged ions moving through a medium are slowed down due to the interaction with charges in the material. In our experiments there is an approximately 20% loss of energy of the ion as it travels through the target. The Coulomb excitation cross sections are very sensitive to the energy of the incoming projectile and in order to take this into account, the cross section needs to be averaged over the distance traveled through the target. It turns out in our case that the loss of energy as a function of distance through the target is very well approximated by linear function. This means that it is sufficient to find the average cross section over the range from the initial to final beam energies. The average total cross section is

$$(\sigma_n)_{\text{av}} = \frac{\int_{E_i}^{E_f} \sigma_n(E) dE}{E_f - E_i}, \quad (4.16)$$

where  $E_i$  and  $E_f$  are the initial and final beam energies, respectively. This calculated average cross section is used in comparing the results of the input matrix elements with the experimentally observed cross sections.

## GOSIA

The second Coulomb excitation program used was GOSIA [55], a program developed by T. Czosnyka, D. Cline and C. Y. Wu at Rochester University. This program allows one to calculate Coulomb excitation cross sections by integrating the coupled differential equations for the Coulomb excitation amplitudes, just as in the CLX program, but it differs in that it also allows one to fit for the transition matrix elements for a given set of measured cross sections and other known spectroscopic data using a minimization procedure. It is also able to take most corrections into account, which are needed to correctly relate the observed  $\gamma$ -ray yields to the transition matrix elements. These corrections include correcting for the change in solid angle and angle due to relativistic effects, accounting for energy loss of ion in the target, and calculation of cross sections from  $\gamma$ -ray yields.

The details of the minimization procedure are given in Ref. [56]. It was found that the transition matrix elements calculated from CLX and GOSIA were consistent within the estimated errors. The GOSIA calculations gave values that were consistently smaller by a small amount than the CLX calculations. The GOSIA calculations were used as consistency check for the CLX calculations. Though GOSIA has the advantage of searching for both positive and negative phases for matrix elements and a method of estimating statistical uncertainties, the GOSIA calculations could not be as thoroughly checked as the CLX calculations and the statistical uncertainties could not be calculated due to lack of experience with the program.

## Measured Transition Strengths

In this section the transition strengths obtained from the Coulomb excitation analysis will be presented. The reduced transition strength is defined as

$$B(\pi\lambda; n \rightarrow m) = \frac{1}{2I_n + 1} |\langle m || \mathcal{M}(\pi\lambda) || n \rangle|^2, \quad (4.17)$$

The collectiveness of a transition can be estimated by the single-particle estimate or Weisskopf unit. For electric transitions, it is defined as

$$B_W(E\lambda) = \frac{(1.2)^{2\lambda}}{4\pi} \left(\frac{3}{\lambda}\right)^2 A^{\frac{2\lambda}{3}} e^2 (\text{fm})^{2\lambda}, \quad (4.18)$$

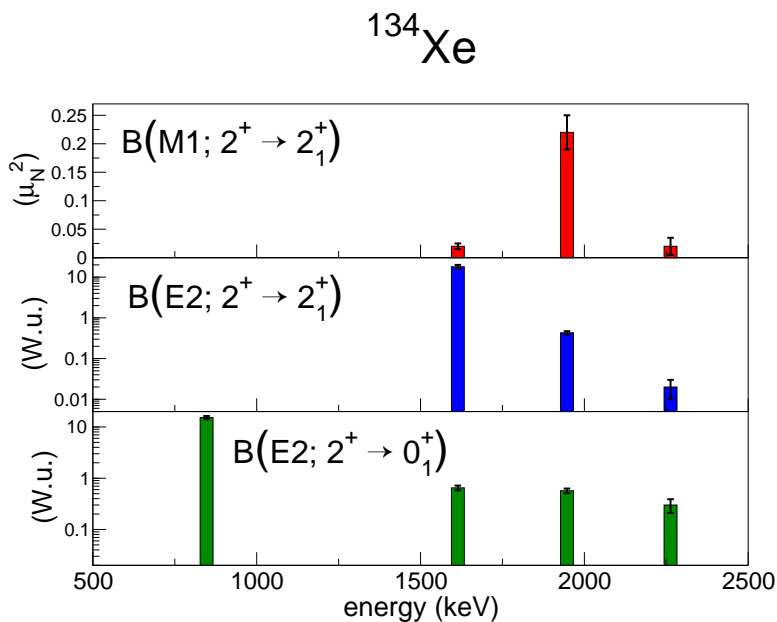


Figure 4.19: The measured transition strengths in  $^{134}\text{Xe}$ . The values plotted for the transitions from the  $2_3^+$  and  $2_4^+$  states are the transition strengths that correspond to the smaller of two possible  $\delta$  values.

where  $A$  is the mass number. For a vibrational nucleus, or nucleus in the  $u(5)$  limit, the collective  $E2$  transitions expected are the ones shown in Fig. 2.3. The collective  $M1$  transition of a  $2_{1,\text{ms}}^+$  mixed-symmetry state is expected to have a transition strength of approximately  $0.2 \mu_N^2$ , which comes from taking the boson  $g$ -factors as  $g_\pi \approx 1$  and  $g_\nu \approx 0$ .

The transition strengths measured in  $^{134}\text{Xe}$  and  $^{136}\text{Ce}$  are given in Tables 4.2 and 4.3, respectively. The transition strengths for electric transition are given in Weisskopf units and the magnetic transitions in  $\mu_N^2$ . Due to the uncertainty due to the two possible values of  $\delta$  calculated for the  $2_3^+ \rightarrow 2_1^+$  and  $2_4^+ \rightarrow 2_1^+$  transitions in  $^{134}\text{Xe}$ , one set of transition strengths were calculated for each  $\delta$  value. The transition strengths for  $^{134}\text{Xe}$  and  $^{136}\text{Ce}$  are plotted in Figs. 4.19 and 4.20, respectively.

#### 4.2.6 Coincidence Analysis

A total of  $2.6 \times 10^6$  and  $2.9 \times 10^6$  events with multiplicity two or higher were recorded for  $^{134}\text{Xe}$  and  $^{136}\text{Ce}$ , respectively. These events were sorted into symmetric  $4096 \times 4096$   $E_\gamma$ - $E_\gamma$  matrices. A two-dimensional view the  $E_\gamma$ - $E_\gamma$  matrix is shown in Fig. 4.21. By gating on observed transitions, one can verify

$E_{\text{level}}$ (keV)	$J^\pi$	$E_\gamma$ (keV)	$J_{\text{final}}^\pi$	$I_\gamma$	$A_2/A_0$	$A_4/A_0$	$\delta$	$B(E2)$ (W.u.)	$B(M1)$ ( $\mu_N^2$ )
847	$2_1^+$	847	$0_1^+$	1.00(1)	0.119(7)	-0.006(9)		15.3(11) <sup>a</sup>	
1614	$2_2^+$	767	$2_1^+$	$4.70(5) \times 10^{-3}$	-0.262(8)	-0.014(11)	-1.5(2)	18(2)	0.020(5)
		1614	$0_1^+$	$4.93(8) \times 10^{-3}$	0.284(11)	-0.059(15)		0.65(7)	
1731	$4_1^+$	884	$2_1^+$	$1.79(2) \times 10^{-3}$				11.6(8) <sup>a</sup>	
1920	$3_1^+$	1073	$2_1^+$	$3.55(5) \times 10^{-4}$			0.16(2) <sup>a</sup>		
1947	$2_3^+$	1100	$2_1^+$	$3.44(4) \times 10^{-3}$	0.265(7)	0.009(10)	0.08(2)	0.43(4) <sup>c</sup>	0.22(3) <sup>c</sup>
							1.86(9)	57(5) <sup>e</sup>	0.068(5) <sup>e</sup>
2263	$2_4^+$	1947	$0_1^+$	$5.15(9) \times 10^{-4}$	0.306 <sup>b</sup>	-0.074 <sup>b</sup>		0.57(6) <sup>c</sup>	
		1415	$2_1^+$	$7.3(1) \times 10^{-4}$	0.326(18)	0.067(24)	0.14(2)	0.02(1) <sup>d</sup>	0.020(15) <sup>d</sup>
2867	$(4)^+$	2263	$0_1^+$	$6.3(1) \times 10^{-4}$	0.322 <sup>b</sup>	-0.091 <sup>b</sup>	1.6(1)	2.2(4) <sup>f</sup>	0.012(1) <sup>f</sup>
		2020	$2_1^+$	$5.9(9) \times 10^{-4}$				0.30(9) <sup>d</sup>	

Table 4.2: A compilation of the measured quantities in  $^{134}\text{Xe}$ .<sup>a</sup>Value from Ref. [57]<sup>b</sup>Calculated values<sup>c</sup>Calculated using value of  $\delta = 0.08(2)$ .<sup>d</sup>Calculated using value of  $\delta = 0.14(2)$ .<sup>e</sup>Calculated using value of  $\delta = 1.86(9)$ .<sup>f</sup>Calculated using value of  $\delta = 1.6(1)$ .

$E_{\text{level}}$ (keV)	$J^\pi$	$\tau$ (ps)	$E_\gamma$ (keV)	$J_{\text{final}}^\pi$	$I_\gamma$	$A_2/A_0$	$A_4/A_0$	$\delta$	$B(E2)$ (W.u.)	$B(M1)$ ( $\mu_N^2$ )
552	$2_1^+$	$9.8(10)^a$	552	$0_1^+$	1.00(4)				$39(4)^a$	
1092	$2_2^+$	5.7(6)	540	$2_1^+$	$6.6(4) \times 10^{-3}$			$-4.7(7)^b$	53(8)	0.002(1)
			1092	$0_1^+$	$2.35(6) \times 10^{-3}$				0.58(8)	
1314	$4_1^+$	$9.5(28)^a$	762	$2_1^+$	$5.5(1) \times 10^{-3}$				$8.0(22)^a$	
2067	$2_3^+$	0.27(1)	1515	$2_1^+$	$6.1(2) \times 10^{-4}$	0.39(1)	-0.02(2)	0.46(8)	0.69(4)	0.022(2)
			2067	$0_1^+$	$7.9(2) \times 10^{-4}$	0.30(1)	-0.10(2)		1.1(7)	
2155	$2_4^+$	0.06(1)	1603	$2_1^+$	$5.0(2) \times 10^{-4}$			$-0.41(8)^b$	3.8(3)	0.17(3)
			2155	$0_1^+$	$4.3(6) \times 10^{-5}$				0.52(3)	

Table 4.3: A compilation of the measured quantities in  $^{136}\text{Ce}$ .<sup>a</sup>Value from Ref. [58]<sup>b</sup>Value from Ref. [54]

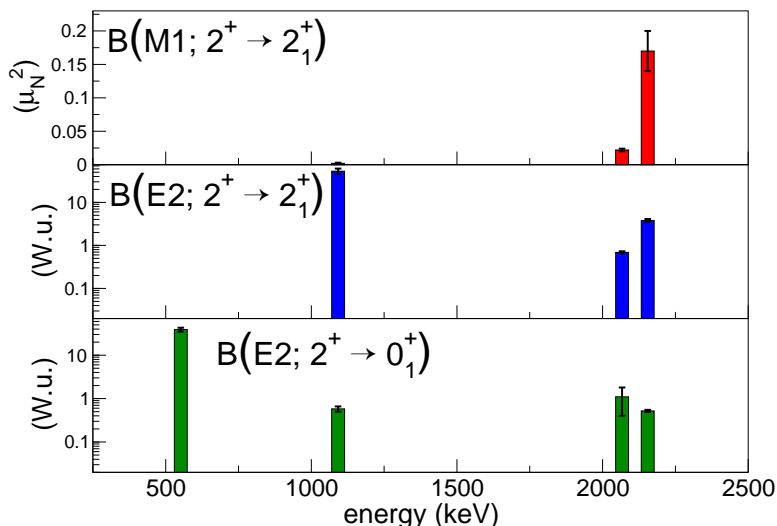
$^{136}\text{Ce}$ 

Figure 4.20: The measured transition strengths in  $^{136}\text{Ce}$ .

the low-energy level scheme for the nuclei of interest and also look for  $\gamma$ -ray transitions that are weak and do not appear in the singles spectrum. An example of a gated spectrum on the 920-keV transition in  $^{134}\text{Xe}$  is shown in Fig. 4.22. The  $\gamma$ -ray transitions in coincidence with the 920-keV transition can clearly be seen.

Evidence for two new  $\gamma$ -ray transitions in  $^{134}\text{Xe}$  were found. A 921-keV transition was found to be in coincidence with the 847-keV and 1100-keV transitions. The proposition that the 921-keV transition connects the 2867-keV state with the 1947-keV state as placed in the level scheme in Fig. 4.6 is supported by the fact that it is consistent with all observed gated spectra. The second new transition observed is the 1254-keV transition connecting the 2867 keV state with the 1614-keV state. It is very close in energy with the 1269-keV transition and both peaks overlap in the observed singles spectrum as can be seen in Fig. 4.4, but it can be seen from the peak width that it is an energy doublet. By gating on the 767-keV or 1614-keV transition, the 1254-keV peak can be clearly isolated in the gated spectrum. It should be noted that the other transitions from the 2867-keV state were not observed in our experiment, thus the transition intensities from the 2867-keV state in our experiment are not consistent with the adopted values of the branching ratios as given in Ref. [57].

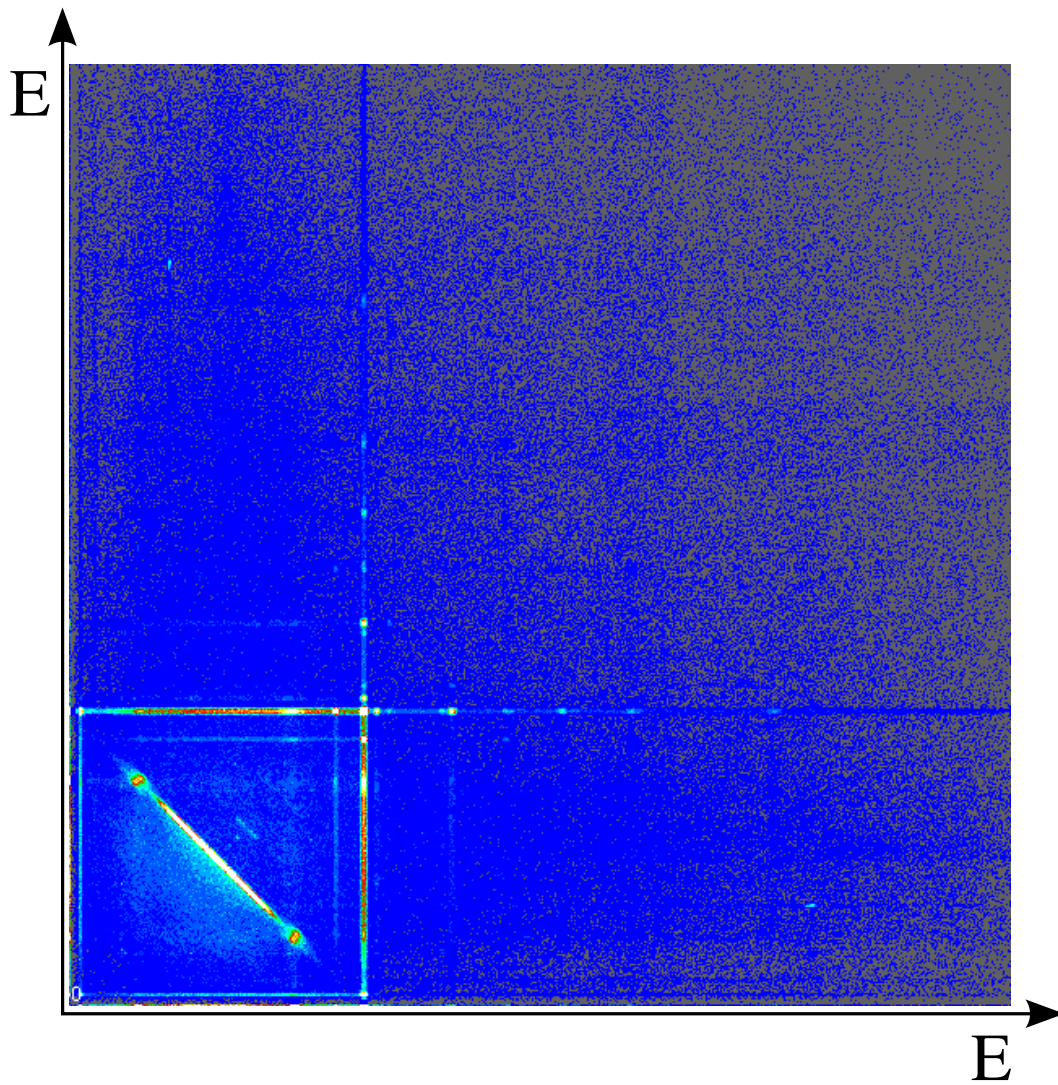


Figure 4.21: A two-dimensional view of the symmetric  $E_\gamma-E_\gamma$  matrix of  $^{134}\text{Xe}$ .



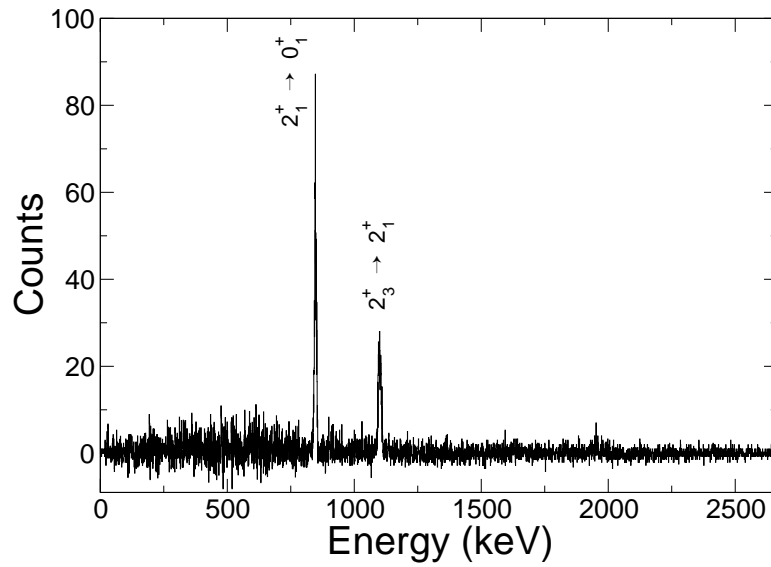


Figure 4.22: A gate on the 921-keV transition in  $^{134}\text{Xe}$ .

From the analysis of the matrix of  $^{136}\text{Ce}$ , one previously unknown  $\gamma$  ray with a measured energy of 1430 keV was found in coincidence with the 552-keV  $2_1^+ \rightarrow 0_1^+$  transition. The placement of this  $\gamma$  ray in the level scheme, if it belongs to  $^{136}\text{Ce}$ , is currently unknown.

# Chapter 5

## Evolution of Mixed-Symmetry States

### 5.1 $N = 80$ Isotones

#### 5.1.1 Identification of the $2_{1,\text{ms}}^+$ State in $^{134}\text{Xe}$

The  $M1$  transitions strengths for  $^{134}\text{Xe}$  are given in Table 4.2. There are two values, each corresponding to the large or small measured value of  $\delta$ . The larger  $M1$  transition of  $B(M1; 2_3^+ \rightarrow 2_1^+) = 0.22(3)$  corresponding to  $\delta = 0.08(2)$  is favored due to the fact that the other possible value of the  $B(M1)$  results in a  $B(E2; 2_3^+ \rightarrow 2_1^+) = 60$  W.u., which is much larger than can be accounted for from any standard description of collective nuclei. Taking the values of the larger  $M1$  transitions for the  $2_3^+ \rightarrow 2_1^+$  and  $2_4^+ \rightarrow 2_1^+$  transitions as can be seen in Fig. 4.19, we find the  $2_3^+$  state is the dominant fragment of the  $2_{1,\text{ms}}^+$  mixed-symmetry state. The uncertainty of the  $B(M1; 2_4^+ \rightarrow 2_1^+)$  value does not affect our conclusion as both possible values are small compared to the  $B(M1; 2_3^+ \rightarrow 2_1^+)$ .

#### 5.1.2 Phenomenological fit

The  $2_{1,\text{ms}}^+$  has been identified in two other  $N = 80$  isotones, namely  $^{136}\text{Ba}$  [27] and  $^{138}\text{Ce}$  [28]. A plot of the energies of the  $2_{1,\text{ms}}^+$  state along with the energies of the  $2_1^+$  state is shown in Fig. 5.1. It can be seen that the energy of the  $2_{1,\text{ms}}^+$  state increases with increasing proton number while the energy of the  $2_1^+$  state decreases with proton number. A simple two-state model was used to reproduce these trends to try to understand the behavior of the splitting in energy between these states.

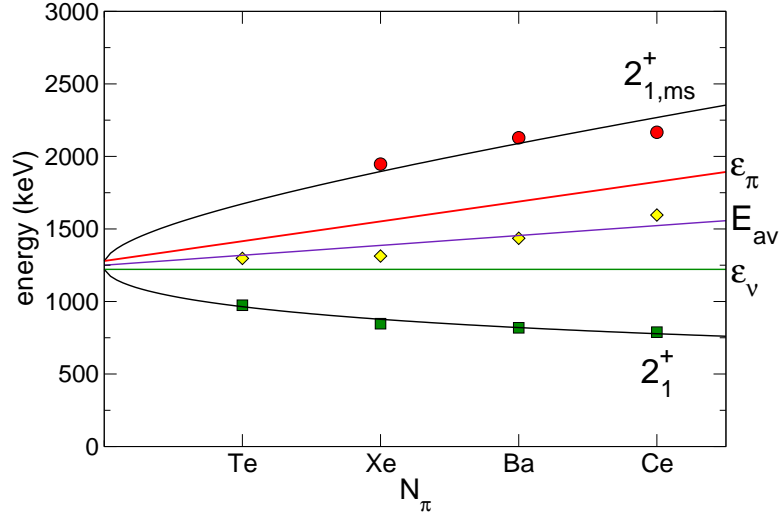


Figure 5.1: A phenomenological fit for the energy of the  $2^+_{1,ms}$  state in the  $N = 80$  isotones

The two-state model is described in Heyde and Sau [20] and uses a proton and neutron  $2^+$  state as the two basis states,

$$|2^+_{\pi}\rangle = \begin{pmatrix} 1 \\ 0 \end{pmatrix} \quad (5.1)$$

$$|2^+_{\nu}\rangle = \begin{pmatrix} 0 \\ 1 \end{pmatrix}. \quad (5.2)$$

The Hamiltonian of the system is

$$H = \begin{pmatrix} \epsilon_{\pi} & V_{\pi\nu} \\ V_{\pi\nu} & \epsilon_{\nu} \end{pmatrix}, \quad (5.3)$$

where  $\epsilon_{\pi}$  and  $\epsilon_{\nu}$  are the energies of the proton and neutron states, respectively, and  $V_{\pi\nu}$  is the interaction between the states. Diagonalizing this Hamiltonian, an eigenstate that is symmetric and anti-symmetric are obtained. The energies of these eigenstates are

$$E_{s,a} = \frac{\epsilon_{\pi} + \epsilon_{\nu}}{2} \mp \frac{1}{2} \sqrt{\frac{\epsilon_{\pi} - \epsilon_{\nu}}{2} - 4V_{\pi\nu}}, \quad (5.4)$$

with the minus sign giving the energies of the symmetric states and the plus sign giving the energy of the anti-symmetric states. It can be seen in Fig. 5.1

that the difference in energy between the  $2_1^+$  state and the  $2_{1,\text{ms}}^+$  state is not constant, but increases. From Heyde and Sau, the interaction is attributed to the proton-neutron quadrupole interaction, which roughly increases as the square root of the product of the number of proton and neutron bosons. We parametrize this interaction as

$$V_{\pi\nu}(N_\pi) = C\sqrt{N_\pi N_\nu}, \quad (5.5)$$

where  $N_\pi$  and  $N_\nu$  are the number proton and neutron bosons, respectively. It can also be seen that the splitting of the experimental energies is not symmetric; the energies of the  $2_{1,\text{ms}}^+$  states seem to increase in energy more quickly than the energies of the  $2_1^+$  states decrease. This can be seen from the average energy  $E_{\text{av}}$ , shown in Fig. 5.1 as the purple line, which increases in energy. In order to reproduce the observed energies, it was assumed that the energies of the proton states increase linearly with proton boson number as a first-order approximation given by

$$\epsilon_\pi(N_\pi) = a + b(N_\pi - 1). \quad (5.6)$$

The fact that the energy of the proton state increases in energy with proton boson number is supported by the fact that the  $2_1^+$  state of the  $N = 82$  isotones increase in energy approximately linearly, shown in Fig. 5.1 as yellow diamonds. Since  $N = 82$  is the neutron shell closure, it is assumed that first excited  $2^+$  state is due mostly to a proton excitation. The form of Eq. (5.6) is chosen such that the parameter  $a$  is the energy of one proton boson, i.e. for  $N_\pi = 1$ . We fix this parameter to the energy of the  $2_1^+$  state in the  $N = 82$  isotope  $^{134}\text{Te}$ . Likewise, we fix the energy of the neutron state to the energy of the  $2_1^+$  state in the  $Z = 50$  nucleus  $^{130}\text{Sn}$ . The  $2_1^+$  state in this nucleus is assumed to arise mainly from the one neutron hole. Thus the values of the fixed parameters are

$$a = E(^{134}\text{Te}; 2_1^+) = 1279 \text{ keV} \quad (5.7)$$

$$\epsilon_\nu = E(^{130}\text{Sn}; 2_1^+) = 1221 \text{ keV}. \quad (5.8)$$

Eq. (5.6) was fit simultaneously to the energies of the  $2_1^+$  and  $2_{1,\text{ms}}^+$  states of the  $N = 80$  isotones using the parameter values given in Eq. (5.7) and (5.8). The results of the fit for the energies of the  $2_1^+$  and  $2_{1,\text{ms}}^+$  are shown as black curves in Fig. 5.1. The energy of the proton state  $\epsilon_\pi(N_\pi)$  is shown as the red curve and the energy of the neutron state  $\epsilon_\nu$ , which remains constant for the isotones, is shown as the green curve. The values of the fitted parameters are  $b = 0.081 \text{ MeV}$  and  $C = 0.341 \text{ MeV}$ .

It can be seen that the fitted energies describe the trends of the isotones quite well showing that this simple parameterization of the  $2_1^+$  and  $2_{1,\text{ms}}^+$  states as a pair of symmetric and anti-symmetric states which come from a basic proton and neutron excitation gives a good qualitative description of the data. Though we can see the increase in the strength of the proton-neutron interaction, this simple model suffers from a deficiency, which is it only takes into account the excitation energies of the states without accounting for the extra binding energy gained from the increasing proton-neutron interaction. In the next section, the fit using the IBM-2 will be presented, which is a more realistic model that accounts for the binding energies resulting from the changing interactions.

### 5.1.3 IBM-2 Calculation

The IBM-2 calculation was performed to reproduce the experimentally observed energies of  $2^+$  states in the  $N = 80$  isotones using the program NPBOS [59]. NPBOS numerically diagonalizes an IBM-2 Hamiltonian using the so called spherical basis, which results from the chain of algebras given in Eq. (2.27). The Hamiltonian used for calculating the eigenstates is

$$H = E_0 + \epsilon_\pi \hat{n}_{d_\pi} + \epsilon_\nu \hat{n}_{d_\nu} + \kappa \hat{Q}_\pi^X \cdot \hat{Q}_\nu^X + \lambda \hat{M}_{\pi\nu}, \quad (5.9)$$

also known as the Talmi Hamiltonian. The multipole operators in the Hamiltonian are defined in Eq. (2.10) and (2.46) and

$$\hat{M}_{\pi\nu} = [s_\nu^\dagger \times d_\pi^\dagger - s_\pi^\dagger \times d_\nu^\dagger]^{(2)} \cdot [\tilde{s}_\nu \times \tilde{d}_\pi - \tilde{s}_\pi \times \tilde{d}_\nu]^{(2)} - 2 \sum_{k=1,3} [d_\nu^\dagger \times d_\pi^\dagger]^{(k)} \cdot [\tilde{d}_\nu \times \tilde{d}_\pi]^{(k)}. \quad (5.10)$$

also called the Majorana operator. The term containing the proton-neutron quadrupole-quadrupole term  $\hat{Q}_\pi^X \cdot \hat{Q}_\nu^X$  is an attractive interaction and is responsible for splitting the  $2_1^+$  and  $2_{1,\text{ms}}^+$  states in energy. The Majorana operator  $\hat{M}_{\pi\nu}$  primarily affects states of mixed-symmetry, increasing their energy.

The parameters in the Hamiltonian were varied by hand until a satisfactory reproduction of the experimental energies was obtained. A sufficient splitting in the energies of the  $2_1^+$  state and the  $2_{1,\text{ms}}^+$  could not be achieved with the proton-neutron quadrupole term alone, hence the inclusion of the Majorana interaction. The energies for the first three  $2^+$  states were calculated and the calculated values are shown in Fig. 5.2. The values of the parameters used in

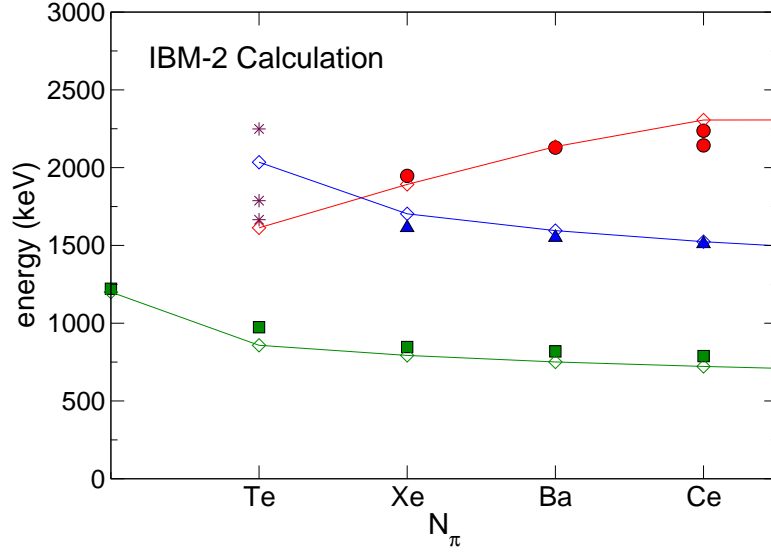


Figure 5.2: Shown are the energies of  $2^+$  states in the  $N = 80$  isotones along with the calculated energy levels using the IBM-2 program NPBOS.

the fit were

$$\begin{aligned}
 \epsilon_\pi &= 0.8 \text{ MeV}, \\
 \epsilon_\nu &= 1.2 \text{ MeV}, \\
 \kappa &= 0.12 \text{ MeV}, \\
 \lambda &= 0.4 \text{ MeV}.
 \end{aligned}
 \tag{5.11}$$

The parameter  $E_0$  was not used as it represents the total binding energy apart from the interactions contained in the Hamiltonian. It can be seen that the trends in the first, second, and third  $2^+$  states are well reproduced with these values. The colored lines connecting the calculated points in Fig. 5.2 represent the grouping of the states depending on whether it is of predominantly fully-symmetric or mixed-symmetry character. The calculation predicts that in  $^{132}\text{Te}$ , the second excited fully-symmetric  $2^+_{2,\text{fs}}$  state and one-phonon  $2^+_{1,\text{ms}}$  mixed-symmetry state have reversed their order in energy. The asterisks indicate the tentative  $2^+$  states in  $^{132}\text{Te}$ , which may correspond to the  $2^+_{2,\text{fs}}$  and  $2^+_{1,\text{ms}}$  state.

There were two aspects of the chosen values of the parameters that were needed to reproduce the energies as shown in Fig. 5.2. First, is the inclusion of both the proton-neutron quadrupole term and the Majorana operator. Second, is the energy of the proton  $d$  boson  $\epsilon_\pi$  needed to be much lower in energy than

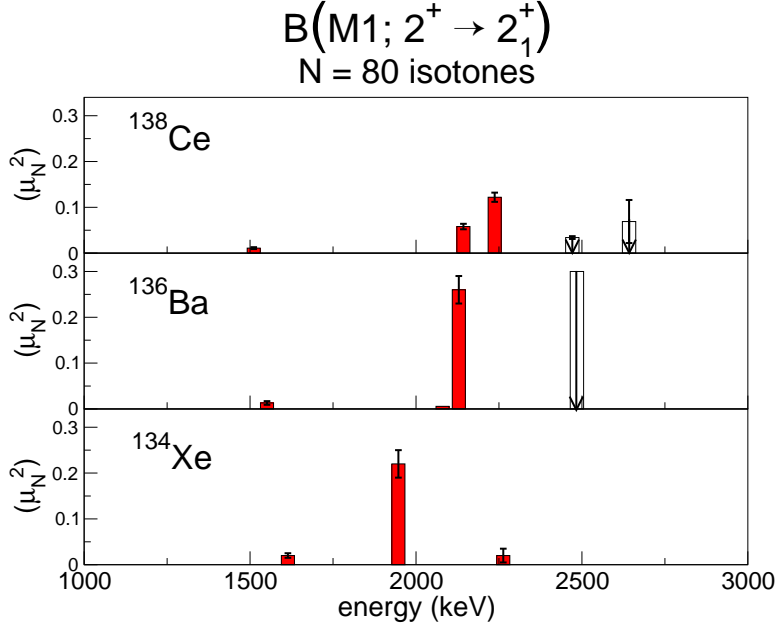


Figure 5.3: The  $M1$  transition strengths are shown for the  $2^+ \rightarrow 2_1^+$  transition in the  $N = 80$  isotones.

the neutron  $d$  boson energy  $\epsilon_\nu$ .

#### 5.1.4 Evolution of Transition Strengths

The measured  $M1$  transition strengths for the  $N = 80$  isotones are plotted in Fig. 5.3. The unfilled bars represent upper limits for the  $M1$  transition strength. For the isotones  $^{134}\text{Xe}$  and  $^{136}\text{Ba}$ , the  $M1$  transition strength is concentrated in the decay of one state, whereas for  $^{138}\text{Ce}$  it is split over two closely-lying  $2^+$  states and is decreased in magnitude. It is suggested by Rainovski et al. [28] that this is due to the filling of the proton  $\pi g_{9/2}$  subshell. Microscopic calculations using the quasiparticle phonon model also suggests that the splitting and decrease in magnitude may be from the effects of the  $\pi g_{9/2}$  subshell [60].

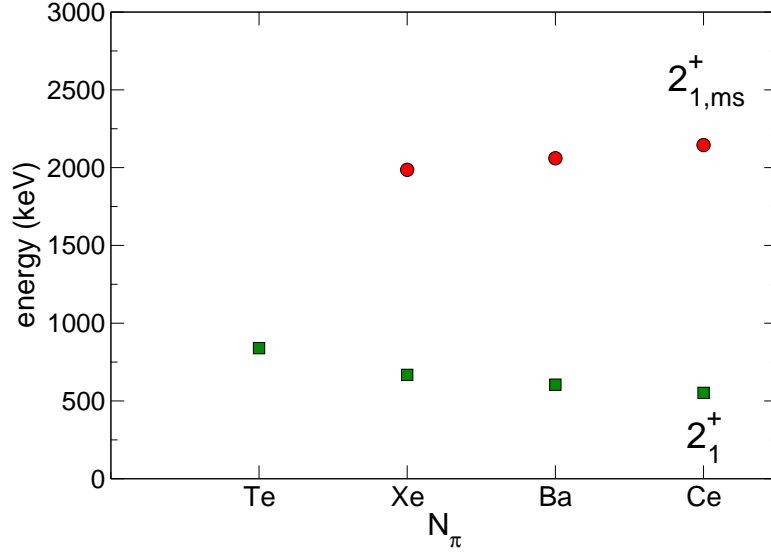


Figure 5.4: The  $2_1^+$  states and  $2_{1,ms}^+$  states of the  $N = 78$  isotones.

## 5.2 $N = 78$ Isotones

### 5.2.1 Identification of the $2_{1,ms}^+$ State in $^{136}\text{Ce}$

From the measured  $M1$  transition strength distribution as given in Table 4.3, the  $2_3^+$  and  $2_4^+$  states are the dominant fragments of the  $2_{1,ms}^+$  state. The energies of the known  $2_{1,ms}^+$  states along with the energies of the  $2_1^+$  states in the  $N = 78$  isotones are shown in Fig. 5.4. It should be noted that the  $2_{1,ms}^+$  state in  $^{132}\text{Xe}$  is only tentatively assigned. It also seems that the splitting in energy between the  $2_1^+$  fully-symmetric states and the  $2_{1,ms}^+$  state increases as a function of proton number. The energy of the  $2_{1,ms}^+$  state appears to increase more slowly with proton number than the ones found in the  $N = 80$  isotones.

### 5.2.2 Evolution of the $2_{1,ms}^+$ State

The  $M1$  transition strengths measured in the  $N = 78$  isotones is plotted in Fig. 5.5. Again, the measurement for  $^{132}\text{Xe}$  is tentative. The total  $M1$  strengths appear to be smaller for the  $N = 78$  isotones when compared to their corresponding isotopes in  $N = 80$ . The  $2_{1,ms}^+$  state is also fragmented in both  $^{134}\text{Ba}$  and  $^{136}\text{Ce}$  while the tentative  $M1$  strengths for  $^{132}\text{Xe}$  indicates that it is not fragmented.



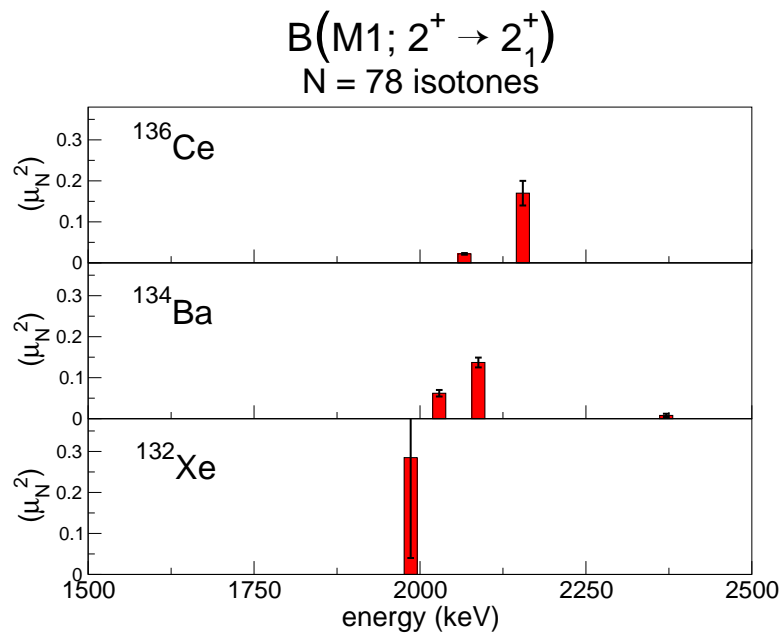


Figure 5.5: The  $M1$  transition strengths for the  $2^+ \rightarrow 2_1^+$  transition in the  $N = 78$  isotones.

# Chapter 6

## Summary

The purpose of this study was to identify and study the properties of MSS's in the  $A = 140$  region. An inverse-kinematics Coulomb excitation experiment was performed to measure absolute transition strengths in  $^{134}\text{Xe}$  and  $^{136}\text{Ce}$ . One-phonon  $2_{1,\text{ms}}^+$  states have been identified in  $^{134}\text{Xe}$  and  $^{136}\text{Ce}$  from measured absolute  $E2$  and  $M1$  transition strengths. By looking at the evolution of the  $2_{1,\text{ms}}^+$  state in the  $N = 80$  isotones, it was found that the energy of the  $2_{1,\text{ms}}^+$  state increases due in part to the proton-neutron interaction. The strength of the proton-neutron interaction has been estimated using two different models resulting in two different values. A model independent way to quantify the strength of the proton-neutron interaction from the properties of the  $2_{1,\text{ms}}^+$  is still needed. The data for the  $2_{1,\text{ms}}^+$  in the  $N = 78$  isotones seems to indicate a similar behavior to the ones in the  $N = 80$  isotones. The confirmation of the  $2_{1,\text{ms}}^+$  state in  $^{132}\text{Xe}$  as well as the identification of the state in neighboring nuclei is needed to further constrain model parameters.

### 6.1 Outlook

The  $2_{1,\text{ms}}^+$  states found so far in the  $A = 140$  mass region give us an interesting glimpse into the behavior of mixed-symmetry states. The extent of the existence of these states and also their purity would test the limits of the validity of describing them as states of mixed proton-neutron symmetry. Efforts are continuing in the search of mixed-symmetry states in this mass region. In June 2006, the same Coulomb excitation experiment was performed at Argonne National Laboratory (ANL) for the rest of the stable Xe isotopes to measure absolute transition strengths. This will allow one to study the  $2_{1,\text{ms}}^+$  along an isotopic chain as one goes farther from the  $N = 82$  shell closure to more collective nuclei at mid-shell. A similar Coulomb excitation experiment

is scheduled to be performed for Sm isotopes where the experiment will probe the deformed region of the nuclear chart for mixed-symmetry states.

Perhaps the measurements that would be the closest to the experiment in our work is ones for the nuclides  $^{130}\text{Te}$  and  $^{132}\text{Te}$  as shown in Fig. 6.1. Measurements in these nuclides would fill the gap that is present for the nuclide between the ones studied and both the  $Z = 50$  and  $N = 82$  shell closures. This may be especially difficult for  $^{132}\text{Te}$  as it is not stable. To date, there has not been any mixed-symmetry states identified in an unstable nuclide. Coulomb excitation experiments are not limited to stable beams. The same type of experiment can be performed using radioactive beams since the projectile is the nuclide of interest. Also allowing the beam to recoil into vacuum would prevent the buildup of radioactivity in the target, which may cause considerable background radiation. Currently, the feasibility of the such an experiment is limited by the availability of high intensity beams as radioactive beam species are much harder to produce. With the plans of high intensity radioactive beam facilities to be available in the near future, such experiment may soon become feasible, which would greatly open the opportunity to identify and study mixed-symmetry states and their evolution in which the Te isotopes are a small example.

	$^{136}\text{Ce}$		$^{138}\text{Ce}$		$^{140}\text{Ce}$
	$^{134}\text{Ba}$		$^{136}\text{Ba}$		$^{138}\text{Ba}$
	$^{132}\text{Xe}$		$^{134}\text{Xe}$		$^{136}\text{Xe}$
	$^{130}\text{Te}$		$^{132}\text{Te}$		$^{134}\text{Te}$
	$^{128}\text{Sn}$		$^{130}\text{Sn}$		$^{132}\text{Sn}$

Figure 6.1: The isotopes  $^{130}\text{Te}$  and  $^{132}\text{Te}$  would extend the known data on mixed-symmetry states in the  $A = 140$  mass region.

# Bibliography

- [1] E. Rutherford. *Philosophical Magazine*, 21:661, 1911.
- [2] J. Chadwick. *Nature*, 129:312, 1932.
- [3] P. A. M. Dirac. *Proc. R. Soc. A*, 117:610, 1928.
- [4] P. A. M. Dirac. *Proc. R. Soc. A*, 118:351, 1928.
- [5] C. Anderson. *Phys. Rev.*, 43:491, 1933.
- [6] G. Gamow. *Proc. R. Soc. A*, 126(803):632–644, 1930.
- [7] C. F. von Weizsäcker. *Zeits. f. Physik*, 96:431, 1935.
- [8] M. Goeppert-Mayer. *Phys. Rev.*, 75:1969, 1949.
- [9] O. Haxel, J. H. D. Jensen, and H. E. Suess. *Zeits. f. Physik*, 128:295, 1950.
- [10] J. Rainwater. *Phys. Rev.*, 79:432, 1950.
- [11] A. Bohr. *Kgl. Danske Videnskab. Selskab, Mat.fys. Medd.*, 26(14), 1952.
- [12] A. Bohr and B. Mottelson. *Kgl. Danske Videnskab. Selskab, Mat.fys. Medd.*, 27(16), 1953.
- [13] D. L. Hill and J. A. Wheeler. *Phys. Rev.*, 89:1102, 1953.
- [14] S. G. Nilsson. *Dan. Mat. Fys. Medd.*, 29(16), 1955.
- [15] A. Arima and F. Iachello. *Phys. Rev. Lett.*, 35:1069, 1975.
- [16] L. Eisenbud and E. P. Wigner. *Nuclear Structure*. Princeton University Press, Princeton, New Jersey, 1958.
- [17] T. Otsuka, A. Arima, and F. Iachello. *Nucl. Phys. A*, 309:1, 1978.

- [18] R. F. Casten, D. S. Brenner, and P. E. Haustein. *Phys. Rev. Lett.*, 58:658, 1987.
- [19] R. B. Cakirli and R. F. Casten. *Phys. Rev. Lett.*, 96:132501, 2006.
- [20] K. Heyde and J. Sau. *Phys. Rev. C*, 33:1050, 1986.
- [21] G. Puddu and O. Scholten. *Nucl. Phys. A*, 348:109, 1980.
- [22] D. Bohle, A. Richter, W. Steffen, A. E. L. Dieperink, N. Lo Iudice, F. Palumbo, and O. Scholten. *Phys. Lett. B*, 137:27, 1984.
- [23] A. Richter. *Prog. Part. Nucl. Phys.*, 34:261, 1995.
- [24] U. Kneissl, H. H. Pitz, and A. Zilges. *Prog. Part. Nucl. Phys.*, 37:349, 1996.
- [25] W. D. Hamilton, A. Irbäck, and J. P. Elliott. *Phys. Rev. Lett.*, 53:2469, 1984.
- [26] N. Pietralla, P. von Brentano, and A. F. Lisetskiy. *Prog. in Part. and Nucl. Phys.*, 60:225, 2008.
- [27] N. Pietralla, D. Belic, P. von Brentano, C. Fransen, R.-D. Herzberg, U. Kneissl, H. Maser, P. Matschinsky, A. Nord, T. Otsuka, H. H. Pitz, V. Werner, and I. Wiedenherver. *Phys. Rev. C*, 58:796, 1998.
- [28] G. Rainovski, N. Pietralla, T. Ahn, C. J. Lister, R. V. F. Janssens, M. P. Carpenter, S. Zhu, and C. J. Barton, III. *Phys. Rev. Lett.*, 96:122501, 2006.
- [29] I. Wiedenhöver, A. Gelberg, T. Otsuka, N. Pietralla, J. Gableske, A. Dewald, and P. von Brentano. *Phys. Rev. C*, 56:R2354, 1997.
- [30] J. R. Vanhoy, J. M. Anthony, B. M. Haas, B. H. Benedict, B. T. Meehan, Sally F. Hicks, C. M. Davoren, and C. L. Lundstedt. *Phys. Rev. C*, 52:2387, 1995.
- [31] S. F. Hicks, C. M. Davoren, W. M. Faulkner, and J. R. Vanhoy. *Phys. Rev. C*, 57:2264, 1998.
- [32] T. C. Li, N. Pietralla, C. Fransen, H. von Garrel, U. Kneisse, C. Kohstall, A. Linnemann, H. H. Pitz, G. Rainovski, A. Richter, M. Scheck, F. Stedile, P. von Brentano, P. von Neumann-Cosel, and V. Werner. *Phys. Rev. C*, 71:044318, 2005.

- [33] W. J. Vermeer, C. S. Lim, and R. H. Spear. *Phys. Rev. C*, 38:2982, 1988.
- [34] F. Iachello and A. Arima. *The Interacting Boson Model*. Cambridge University Press, Cambridge, 1987.
- [35] A. Bohr and B. Mottelson. *Nuclear Structure*, volume I. W. A. Benjamin, Inc., New York, 1969.
- [36] A. Arima, T. Otsuka, F. Iachello, and I. Talmi. *Phys. Lett. B*, 66:205, 1977.
- [37] L. C. Biedenharn and P. J. Brussard. *Coulomb Excitation*. Oxford University Press, Amen House, London, E.C.4, 1965.
- [38] K. Alder, A. Bohr, T. Huus, B. Mottelson, and A. Winther. *Rev. Mod. Phys.*, 28:432, 1956.
- [39] K. Alder and A. Winther. *Electromagnetic Excitation*. North-Holland Publishing Co., Amsterdam, 1975.
- [40] D. Cline. *Ann. Rev. Nuc. Part. Sci.*, 36:683, 1986.
- [41] A. Winther and J. de Boer. A computer program for multiple coulomb excitation. In K. Alder and A. Winther, editors, *Coulomb Excitation*, page 303. Academic Press Inc., New York, 1966.
- [42] K. Alder and A. Winther. *Kgl. Danske Videnskab. Selskab, Mat.fys. Medd.*, 32(8), 1960.
- [43] H. Ower. PhD thesis, Johann-Wolfgang-Goethe-Universität zu Frankfurt am Main, 1980.
- [44] A. Lell. Master's thesis, Universität München, 1978.
- [45] L. C. Biedenharn and M. E. Rose. *Rev. Mod. Phys.*, 24:249, 1953.
- [46] H. Frauenfelder and R. M. Steffen. Angular distribution of nuclear radiation. In K. Siegbahn, editor, *Alpha-, Beta-, and Gamma-ray Spectroscopy*, volume 2, chapter XIXA, pages 997–1198. North-Holland Pub. Co., Amsterdam, 1965.
- [47] R. M. Steffen and K. Adler. Angular distributions and correlations of gamma rays—i. theory. In W. D. Hamilton, editor, *The Electromagnetic Interaction in Nuclear Physics*, chapter XII. North-Holland Pub. Co., Amsterdam, 1972.

- [48] I.-Y. Lee. *Nucl. Phys. A*, 520:641, 1990.
- [49] P.J. Nolan, F.A. Beck, and D.B. Fossan. *Annu. Rev. Nucl. Part. Sci.*, 45:561, 1994.
- [50] M. A. Riley. Gammasphere, the beginning...1993-1997. Dept. of Physics, Florida State University. URL <http://nucalf.physics.fsu.edu/~riley/gamma/>.
- [51] W. F. Mueller, J. A. Church, T. Glasmacher, D. Gutknecht, G. Hackman, P. G. Hansen, Z. Hu, K. L. Miller, and P. Quirin. *Nucl. Instr. and Meth. in Phys. Res. A*, 466:492, 2001.
- [52] D. Pelte and D. Schwalm. In-beam gamma-ray spectroscopy with heavy ions. In R. Bock, editor, *Heavy Ion Collisions*, volume 3, chapter 1, page 1. North-Holland Pub. Co., Amsterdam, 1982.
- [53] T. Yamazaki. *Nucl. Data*, 3:1, 1967.
- [54] T. Ahn, N. Pietralla, G. Rainovski, A. Costin, K. Dusling, T. C. Li, A. Linnemann, and S. Pontillo. *Phys. Rev. C*, 75:014313, 2007.
- [55] T. Czosnyka, D. Cline, and C. Y. Wu. *Am. Phys. Soc.*, 28:745, 1983.
- [56] T. Czosnyka, D. Cline, and C. Y. Wu. *Coulomb Excitation Data Analysis Code; GOSIA*. Dept. of Physics and Astronomy, University of Rochester, April 2008.
- [57] A. A. Sonzogni. *Nucl. Data Sheets*, 103:1, 2004.
- [58] A. A. Sonzogni. *Nucl. Data Sheets*, 95:837, 2002.
- [59] T. Otsuka and N. Yoshida. *User's Manual of the Program NPBOS*. Tokai Research Establishment, JAERI, June 1985.
- [60] N. Lo Iudice, C. Stonyanov, and D. Tarpanov. submitted for publication.
- [61] K. S. Krane and R. M. Steffen. *Phys. Rev. C*, 2:724, 1970.
- [62] H. J. Rose and D. M. Brink. *Rev. Mod. Phys.*, 39:306, 1967.
- [63] K. S. Krane, R. M. Steffen, and R. M. Wheeler. *Nucl. Data Tables*, 11:351, 1973.



# Appendix A

## Multipole Operators and Mixing Ratios

In this appendix, some expressions describing emission of electromagnetic radiation as well as some of the different definitions of the multipole mixing ratio used in the literature will be presented. Detailed discussions of  $\gamma$  radiation can be found for example in Refs. [35] and [52]. The much of the discussion on multipole moments follows that of Chap. 3C-2 of the former.

### A.1 Gamma Emission

Electromagnetic waves are described by the well known Maxwell's equations. The creation and annihilation of radiation can be attributed to the magnetic vector potential  $\mathbf{A}(\mathbf{r})$ . Photons can exist in two polarization states, which is related to the two possible helicities of the photon, i.e. whether the photon's spin is projected parallel or anti-parallel to its propagation direction. Another possible way to describe the two polarizations is through the photon's parity. For a photon with momentum  $q$  and angular momentum quantum numbers  $\lambda\mu$ , its parity can take values  $\pi = \pm 1$ , each of which corresponds to a linear combination of states with a helicity of  $h = \pm 1$ . Photons characterized by  $\pi$  and  $\lambda$  can be classified as either electric ( $E\lambda$ ) or magnetic ( $M\lambda$ ) multipole quanta. The parity of the photons is given by

$$\pi = \begin{cases} (-1)^\lambda & \text{for } E\lambda \text{ with } \kappa = \lambda \pm 1 \\ (-1)^{\lambda+1} & \text{for } M\lambda \text{ with } \kappa = \lambda \end{cases} \quad (\text{A.1})$$

where  $\kappa$  is the orbital angular momentum of the photon.

The two polarization states of a photon can be described using the gauge

$$\nabla \cdot \mathbf{A} = 0 \quad (\text{A.2})$$

from which the multipole operators for electric and magnetic transitions can be defined as

$$\mathcal{M}(E\lambda, \mu) = \frac{-i(2\lambda + 1)!!}{cq^{\lambda+1}} \int \mathbf{j}(\mathbf{r}) \cdot \nabla \times (\mathbf{r} \times \nabla)(j_\lambda(qr)Y_{\lambda\mu}(\hat{\mathbf{r}}))d\tau, \quad (\text{A.3})$$

$$\mathcal{M}(M\lambda, \mu) = \frac{-(2\lambda + 1)!!}{cq^\lambda(\lambda + 1)} \int \mathbf{j}(\mathbf{r}) \cdot (\mathbf{r} \times \nabla)(j_\lambda(qr)Y_{\lambda\mu}(\hat{\mathbf{r}}))d\tau. \quad (\text{A.4})$$

### Long wavelength approximation

The spherical Bessel functions  $j_\lambda(qr)$  can be expanded as

$$j_\lambda(qr) = \frac{(qr)^\lambda}{(2\lambda + 1)!!} \left( 1 - \frac{1}{2} \frac{(qr)^2}{2\lambda + 3} + \dots \right). \quad (\text{A.5})$$

The wavelengths of  $\gamma$  radiation emitted from excited nuclear states are typically much longer than the radius of nucleus. For this condition of  $qr \ll 1$ , it is sufficient to take the first term of the expansion. This results in the following forms for the multipole operators,

$$\mathcal{M}(E\lambda, \mu) = \int \rho(\mathbf{r})r^\lambda Y_{\lambda\mu}(\hat{\mathbf{r}})d\tau, \quad (\text{A.6})$$

$$\mathcal{M}(M\lambda, \mu) = \frac{-1}{c(\lambda + 1)} \int \mathbf{j}(\mathbf{r}) \cdot (\mathbf{r} \times \nabla)r^\lambda Y_{\lambda\mu}(\hat{\mathbf{r}})d\tau. \quad (\text{A.7})$$

### Transition Strengths and Rates

The reduced transition strength is defined as

$$\begin{aligned} B(E(M)\lambda; I_1 \rightarrow I_2) &= \sum_{\mu M_2} |\langle I_2 M_2 | \mathcal{M}(E(M)\lambda, \mu) | I_1 M_1 \rangle|^2 \\ &= \frac{1}{(2I_1 + 1)} |\langle I_2 || \mathcal{M}(E(M)\lambda) || I_1 \rangle|^2, \end{aligned} \quad (\text{A.8})$$

where  $\langle I_2 || \mathcal{M}(E(M)\lambda) || I_1 \rangle$  is the reduced matrix element. The transition rate or intensity of the radiation of multipole  $L$  is given by

$$T(E(M)\lambda; I_1 \rightarrow I_2) = \frac{8\pi(\lambda + 1)}{\lambda[(2\lambda + 1)!!]^2} \frac{1}{\hbar} q^{2\lambda+1} B(E(M)\lambda; I_1 \rightarrow I_2). \quad (\text{A.9})$$

This is related to the expression found in Eq. 3.23 by

$$T(E(M)\lambda; I_1 \rightarrow I_2) = [\Delta(\lambda)(I_1 \rightarrow I_2)]^2. \quad (\text{A.10})$$

## A.2 Multipole Mixing Ratios

Discussions on  $\gamma\gamma$  angular correlations, angular distributions, and the definitions of multipole operators and their corresponding multipole mixing ratios can be found in Refs. [35, 45, 47, 61–63]. Here only a few of the expressions for the multipole mixing ratios often found in the literature will be given.

A commonly used definition of the multipole mixing ratio given by Krane et al. [61, 63] is

$$\delta = \frac{\langle I_2 \parallel \mathbf{j}(\mathbf{r}) \cdot \mathbf{A}_{\lambda'}^{(\pi')} \parallel I_1 \rangle}{\langle I_2 \parallel \mathbf{j}(\mathbf{r}) \cdot \mathbf{A}_{\lambda}^{(\pi)} \parallel I_1 \rangle}, \quad (\text{A.11})$$

where  $\mathbf{j}(\mathbf{r})$  is the nuclear current operator and the multipole fields are given by

$$\mathbf{A}_{\lambda\mu}^{(M)}(q, \mathbf{r}) = i^\lambda \frac{\mathbf{L}}{[\lambda(\lambda+1)]^{\frac{1}{2}}} j_\lambda(qr) Y_{\lambda\mu}(\hat{\mathbf{r}}) \quad (\text{A.12})$$

and

$$\mathbf{A}_{\lambda\mu}^{(E)}(q, \mathbf{r}) = \frac{i^\lambda}{q} \frac{\nabla \times \mathbf{L}}{[\lambda(\lambda+1)]^{\frac{1}{2}}} j_\lambda(qr) Y_{\lambda\mu}(\hat{\mathbf{r}}), \quad (\text{A.13})$$

using the natural units  $c = \hbar = m = 1$  and where  $\mathbf{L}$  is the angular momentum operator,  $j_\lambda(qr)$  are the spherical Bessel functions, and  $Y_{\lambda\mu}(\hat{\mathbf{r}})$  are the spherical harmonics. The reduced matrix elements are defined by the Wigner-Eckart theorem as

$$\begin{aligned} \langle I_2 M_2 \mid \mathbf{j}(\mathbf{r}) \cdot \mathbf{A}_{\lambda\mu}^{(\pi)*} \mid I_1 M_1 \rangle &= (-1)^{\lambda-\mu+1} \langle I_2 M_2 \mid \mathbf{j}(\mathbf{r}) \cdot \mathbf{A}_{\lambda-\mu}^{(\pi)} \mid I_1 M_1 \rangle \\ &= (-1)^{\lambda-\mu+1} (-1)^{I_2-M_2} \begin{pmatrix} I_2 & \lambda & I_1 \\ -M_2 & -\mu & M_1 \end{pmatrix} \langle I_2 \parallel \mathbf{j}(\mathbf{r}) \cdot \mathbf{A}_{\lambda\mu}^{(\pi)} \parallel I_1 \rangle \end{aligned} \quad (\text{A.14})$$

where  $\begin{pmatrix} I_2 & \lambda & I_1 \\ -M_2 & -\mu & M_1 \end{pmatrix}$  is the Wigner 3- $j$  symbol.

The relation between the reduced matrix elements given in Eq. (A.14) and the ones found in the reduced transition strengths as in Eq. (A.8) is given by

$$\langle I_2 \parallel \mathbf{j}(\mathbf{r}) \cdot \mathbf{A}_{\lambda}^{(E)} \parallel I_1 \rangle = \frac{q^\lambda}{(2\lambda+1)!!} \left( \frac{\lambda+1}{\lambda} \right)^{\frac{1}{2}} \langle I_2 \parallel i^\lambda \mathcal{M}(E\lambda) \parallel I_1 \rangle \quad (\text{A.15})$$

for electric transitions and

$$\langle I_2 \parallel \mathbf{j}(\mathbf{r}) \cdot \mathbf{A}_\lambda^{(M)} \parallel I_1 \rangle = -\frac{q^\lambda}{(2\lambda+1)!!} \left( \frac{\lambda+1}{\lambda} \right)^{\frac{1}{2}} \langle I_2 \parallel i^{\lambda-1} \mathcal{M}(M\lambda) \parallel I_1 \rangle \quad (\text{A.16})$$

for magnetic transitions. Using these relations, one obtains the expression for the  $E2/M1$  multipole mixing ratio defined previously in Eq. (4.11) as

$$\delta = q \frac{\sqrt{3} \langle I_2 \parallel \mathcal{M}(\pi'\lambda') \parallel I_1 \rangle}{10 \langle I_2 \parallel \mathcal{M}(\pi\lambda) \parallel I_1 \rangle}. \quad (\text{A.17})$$

The use of both the multipole operators defined by Eqs. (A.6) and (A.7), and Eqs. (A.12) and (A.13) and their corresponding matrix elements in defining the multipole mixing ratios can be a source of confusion when they are unknowingly interchanged.

Another definition of the multipole operators  $\mathcal{T}_{\lambda\mu}^{(\pi)}$  by Rose and Brink [62] leads to reduced transition matrix elements related to the ones defined Eq. (A.14) by

$$\langle I_2 \parallel \mathbf{j}(\mathbf{r}) \cdot \mathbf{A}_\lambda^{(M)} \parallel I_1 \rangle = (-1)^{I_1-I_2+\lambda} \left[ \frac{2I_1+1}{2\pi(2\lambda+1)} \right]^{\frac{1}{2}} \langle I_1 \parallel \mathcal{T}_\lambda^{(\pi)} \parallel I_2 \rangle. \quad (\text{A.18})$$

The seldom used definition of a multipole mixing ratio using the multipole operators  $\mathcal{M}(\pi\lambda)$  is given by

$$\delta' = \frac{\langle I_2 \parallel \mathcal{M}(\pi'\lambda') \parallel I_1 \rangle}{\langle I_2 \parallel \mathcal{M}(\pi\lambda) \parallel I_1 \rangle}, \quad (\text{A.19})$$

with the matrix elements for electric transitions given in  $e(\text{fm})^\lambda$  and matrix elements for magnetic transitions given in  $\mu_N(\text{fm})^{\lambda-1}$ .